



UNIwersytet Technologiczno-Przyrodniczy  
IM. JANA I JĘDRZEJA ŚNIADECKICH  
W BYDGOSZCZY

ZESZYTY NAUKOWE NR 251

# ELEKTROTECHNIKA

# 13

WYDZIAŁ TELEKOMUNIKACJI  
I ELEKTROTECHNIKI



BYDGOSZCZ – 2008



UNIwersytet Technologiczno-Przyrodniczy  
IM. JANA I JĘDRZEJA ŚNIADECKICH  
W BYDGOSZCZY

**ZESZYTY NAUKOWE NR 251**

**ELEKTROTECHNIKA**

**13**

*C<sub>2</sub>*  
*1905*

BYDGOSZCZ – 2008

REDAKTOR NACZELNY  
prof. dr hab. inż. Janusz Prusiński

REDAKTOR DZIAŁOWY  
dr inż. Sławomir Cieślik

OPRACOWANIE TECHNICZNE  
mgr inż. Daniel Morzyński

© Copyright  
Wydawnictwa Uczelniane Uniwersytetu Technologiczno-Przyrodniczego  
Bydgoszcz 2008

ISSN 0209-0570

Wydawnictwa Uczelniane Uniwersytetu Technologiczno-Przyrodniczego  
ul. Ks. A. Kordeckiego 20, 85-225 Bydgoszcz, tel. (052) 3749482, 3749426  
e-mail: [wydawucz@utp.edu.pl](mailto:wydawucz@utp.edu.pl) <http://www.utp.edu.pl/~wyd>

---

Wyd. I. Nakład 80 egz. Ark. aut. 3,0. Ark. druk. 3,5.  
Zakład Małej Poligrafii UTP Bydgoszcz, ul. Ks. A. Kordeckiego 20

## Contents

1. Jacek F. Gieras – Analytical prediction of noise of magnetic origin produced by permanent magnet brushless motors .....5
2. Jacek F. Gieras, Jae-Hyuk Oh, Mihai Huzmezan – Electromechanical portable energy harvesting device: analysis and experimental tests .....17
3. Roman Żarnowski – Presentation of the DC machine simultaneously but separately controlled by two voltages using the state-space method .....37



## ANALYTICAL PREDICTION OF NOISE OF MAGNETIC ORIGIN PRODUCED BY PERMANENT MAGNET BRUSHLESS MOTORS

Jacek F. Gieras

University of Technology and Life Sciences  
Al. S. Kaliskiego 7, 85-796 Bydgoszcz, Poland  
e-mail: jgieras@iee.org

*Summary:* Prediction of acoustic noise radiated by electric motors is nowadays important both for machine manufacturers and users. This paper describes an engineering approach to prediction of noise of magnetic origin produced by permanent magnet (PM) brushless motors. The sound power level (SWL) is calculated on the basis of magnetic field analysis in the air gap, radial forces, natural frequencies of the stator-frame system and radiation efficiency coefficient. Accuracy problems encountered in the analytical and numerical noise prediction have been discussed.

*Keywords:* permanent magnets, brushless motors, noise, magnetic field

### 1. INTRODUCTION

Although the noise and vibration of induction machines have widely been discussed in many references, e.g. [1-6], significantly less research activity has been observed in vibro-acoustics of permanent magnet (PM) brushless motors, e.g. [7-10].

Noise and vibration produced by electrical machines can be divided into three categories:

- magnetic vibration and noise associated with parasitic effects due to higher space and time harmonics of magnetic field, eccentricity, phase unbalance, slot openings, magnetic saturation, and magnetostrictive expansion of the core laminations;
- mechanical vibration and noise associated with the mechanical assembly, in particular bearings;
- aerodynamic vibration and noise associated with flow of ventilating air through or over the motor.

This paper deals only with the noise of magnetic origin produced by radial magnetic forces due to magnetic flux density waveforms in the air gap. The paper also does not discuss the load induced noise, i.e., noise due to coupling the machine with a mechanical load and due to mounting the machine on foundation or other structure.

## 2. ENERGY CONVERSION PROCESS

Fig. 1a. shows how the electrical energy is converted into acoustic energy in an electric machine. The input current interacts with the magnetic field producing high-frequency forces that act on the inner stator core surface (Fig. 1b). These forces excite the stator core and frame in the corresponding frequency range and generate mechanical vibration and noise. As a result of vibration, the surface of the stator yoke and frame displaces with frequencies corresponding to the frequencies of forces. The surrounding medium (air) is excited to vibrate too and generates acoustic noise.

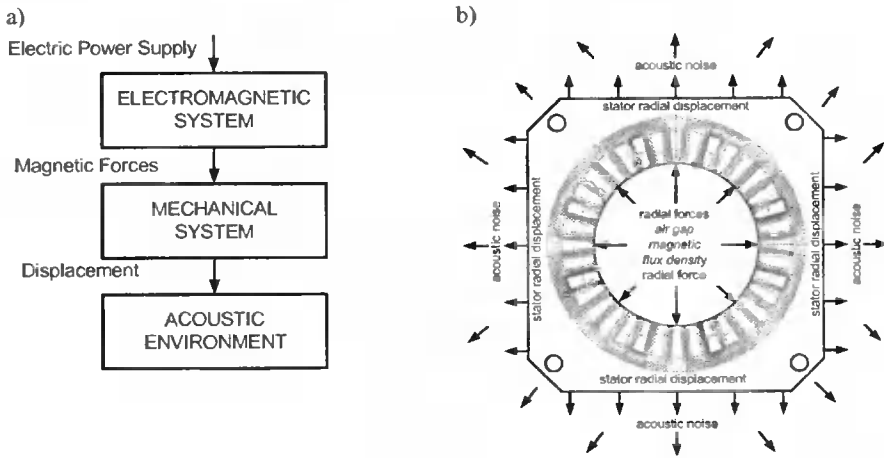


Fig. 1. Generation of vibration and noise in electric machines: (a) conversion of electric energy into acoustic energy; (b) excitation of the stator and frame to vibrate by radial magnetic forces.

The acoustic power radiated from the frame is a very small fraction of the electrical input power. The sound power level (SWL) of 100 dB corresponds to the power of 0.01 W, while 60 dB corresponds to the power of  $10^{-6}$  W. Among other things, this causes a low accuracy of calculation of the SWL.

The stator and frame assembly, as a mechanical system, is characterized by a distributed mass  $M$ , damping  $C$  and stiffness  $K$ . The magnetic force waves excite the mechanical system to generate vibration. The amplitude of vibration is a function of the magnitude and frequency of these forces as well as parameters  $M$ ,  $C$  and  $K$ .

## 3. DETERMINISTIC AND STATISTICAL METHODS OF NOISE PREDICTION

In the *analytical* and *numerical* approach, usually, a *deterministic* method is employed. As shown in Fig. 1a, the magnetic forces acting on a motor structure have to be calculated from the input currents and voltages using an analytical *electromagnetic model* [8, 9] or the FEM model [8, 11]. The vibration characteristics are then determined using a *structural model* normally based on the FEM [7, 8, 11-13]. By using the vibration velocities of the motor structure predicted from the *structural model*, the radi-

ated sound power level can then be calculated on the basis of an *acoustic model*. The acoustic model may be formulated using either the FEM or boundary-element method (BEM). The FEM/BEM, by their nature, are limited to low frequencies.

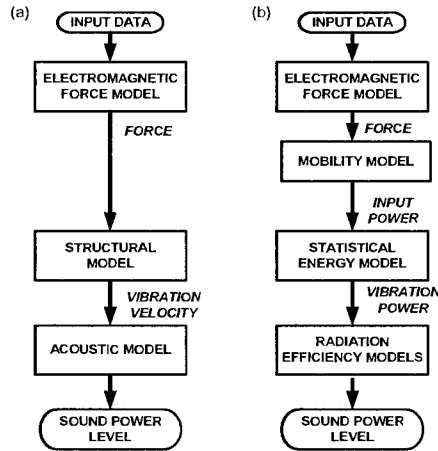


Fig. 2. Flowcharts for noise prediction: (a) deterministic method; (b) statistical method.

A method that is particularly suitable for calculations of noise and vibration at high frequencies is the so-called *statistical energy analysis* (SEA), which has been applied with success to a number of mechanical systems such as ship, car, and aircraft structures [14]. This method was first applied to electrical motors in 1999 [12, 13, 15]. The method basically involves dividing a structure (such as a motor) into a number of subsystems and writing the energy balance equations for each subsystem, thus allowing the statistical distribution of energies over various frequency bands to be determined. The main advantage of the statistical approach (Fig. 2b) is that it does not require all the details to be modeled.

#### 4. ELECTROMAGNETIC SOURCES OF NOISE

Electromagnetic vibration and noise are caused by magnetic flux density waves in the air gap. If the stator produces  $b_{1v}(\alpha, t) = B_{mv} \cos(v p \alpha \mp \omega_v t + \phi_v)$  magnetic flux density wave and rotor produces  $b_{2\mu}(\alpha, t) = B_{m\mu} \cos(\mu p \alpha \mp \omega_\mu t + \phi_\mu)$  magnetic flux density wave, then the magnetic pressure on the inner surface of the stator core is:

$$\begin{aligned}
 p_{rv} &= \frac{[b_{1v}(\alpha, t) + b_{2\mu}(\alpha, t)]^2}{2\mu_0} = \frac{B_{mv}^2}{4\mu_0} [1 + \cos(2v p \alpha \mp 2\omega_v t + 2\phi_v)] + \\
 &+ \frac{B_{mv} B_{m\mu}}{2\mu_0} \left\{ \cos[p(v - \mu)\alpha \mp (\omega_v - \omega_\mu)t + (\phi_v - \phi_\mu)] + \right. \\
 &\left. + \cos[p(v + \mu)\alpha \mp (\omega_v + \omega_\mu)t + (\phi_v + \phi_\mu)] \right\} + \frac{B_{m\mu}^2}{4\mu_0} [1 + \cos(2\mu p \alpha + 2\omega_\mu t + 2\phi_\mu)]
 \end{aligned} \tag{1}$$



where  $B_{mv}$  and  $B_{m\mu}$  are the amplitudes of the stator and rotor magnetic flux density waves,  $\omega_v$  and  $\omega_\mu$  are the angular frequencies of the stator and rotor magnetic fields,  $p$  is the number of pole pairs,  $\omega_s$  and  $\omega_r$  are phases of the stator and rotor magnetic flux density waves,  $v = 1, 5, 7, 11, 13, \dots$  for three phase machines, and  $\mu = 1, 3, 5, \dots$ . The amplitudes of magnetic stress (or magnetic pressure) waves in the air gap are:

$$P_{mv} = \frac{1 B_{mv}^2}{4 \mu_0}, \quad P_{mv\mu} = \frac{1 B_{mv} B_{m\mu}}{2 \mu_0} \quad \text{and} \quad P_{m\mu} = \frac{1 B_{m\mu}^2}{4 \mu_0} \quad (2)$$

Their frequencies are  $\omega_r = 2\omega_v$ ,  $\omega_r = \omega_v \mp \omega_\mu$ , or  $\omega_r = 2\omega_\mu$  orders  $r = 2vp$ ,  $r = (v \mp \mu)p$  or  $r = 2\mu p$  ( $r = 0, 1, 2, 3, \dots$ ) and phases  $\phi_r = 2\phi_v$ ,  $\phi_r = \phi_v \mp \phi_\mu$  or  $\phi_r = 2\phi_\mu$ . The magnetic stress wave acts in radial directions on the stator core and rotor core active surfaces causing the deformation and, hence, the vibration and noise. Frequencies and orders (circumferential modes) of all fundamental radial magnetic forces are given in Table 1 where  $f$  is the frequency of the stator current.

Table 1. Frequencies of radial magnetic forces produced by higher space harmonics  $v > 1$  in PM brushless (synchronous) motors ( $s_1$  is the number of stator slots and  $m_1$  is the number of phases).

Source	Frequency Hz	Order (circumferential mode)
Product of stator space harmonics $b_v^2$ of the same number $v$	$f_r = 2f$	$r = 2vp$ $r = 2km_1 \pm 1$ $k = 0, 1, 2, 3, \dots$
Interaction of the rotor magnetic field and slotted core of the stator	$f_r = 2\mu_s f$ where $\mu_s = \text{integer } [s_1/p]$	$r = 2(\mu_s p \pm s_1)$
Product of rotor space harmonics $b_\mu^2$ of the same number $\mu$	$f_r = 2(1 \pm 2k)f$	$r = 2\mu p = 2p(1 \pm 2k)$ where $\mu = 1 \pm 2k$
Product of stator and rotor space harmonics $b_s b_r$ — general equations	$f_r = f \pm f_\mu$	$r = (v \pm \mu)p$
Product of stator winding and rotor space harmonics $b_s b_r$ where $v = ks_1/p \pm 1$ and $\mu = 2k \pm 1$	$f_r = 2(1+k)f$ $f_r = 2kf$	$r = ks_1 \pm 2p(1+k)$
Product of stator and rotor static eccentricity space harmonics $b_s b_r$	$f_r = 2(1+k)f$ $f_r = 2kf$	$r = 1$ $r = 2$
Product of stator and rotor dynamic eccentricity space harmonics $b_s b_r$	$f_r = [2(1+k) \pm 1/p]f$ $f_r = (2k \pm 1/p)f$	$r = 1$ $r = 2$
Product of stator and rotor magnetic saturation space harmonics $b_s b_\mu$	$f_r = 2(2+k)f$ $f_r = 2(1+k)f$	$r = ks_1 + 2p(k+2)$ $r = ks_1 + 2p(k+1)$

The magnetomotive force (MMF) space harmonics, time harmonics, slot harmonics, eccentricity harmonics, and saturation harmonics produce parasitic higher harmonic forces and torques. The amplitude of the radial force of the order  $r$  is  $F_{mr} = \pi D_{in} L_i P_{mr}$  where  $D_{in}$  is the stator core inner diameter,  $L_i$  is the effective length of the core and  $P_{mr}$  is the amplitude of the radial magnetic pressure according to eqn (2).

The stator – frame (or stator – enclosure) structure is the main radiator for the machine noise. If the frequency of the radial force is close to or equal to any of the natural frequencies of the stator – frame system, a resonance occurs, leading to the stator system deformation, vibration, and acoustic noise.

Magnetostrictive noise of electrical machines with number of poles  $2p > 4$  can be neglected due to low frequency  $2f$  and high order  $r = 2p$  of radial forces. However, radial forces due to the magnetostriction effect can reach about 50% of radial forces produced by the air gap magnetic field.

In inverter fed motors, parasitic oscillating torques are produced due to higher time harmonics in the stator winding currents. These parasitic torques are, in general, greater than oscillating torques produced by space harmonics. Moreover, the voltage ripple of the rectifier is transmitted through the intermediate circuit to the inverter and produces another kind of oscillating torque [3].

## 5. ENGINEERING APPROACH TO PREDICTION OF NOISE

Although, the analytical and FEM/BEM numerical approaches seem to work well, the time consuming preprocessing and computations can be a drawback to use this approach in engineering practice. On the other hand, it is relatively easy to write a *Mathcad*<sup>1</sup> or *Mathematica*<sup>2</sup> computer program for fast prediction of the SWL spectrum generated by magnetic forces using analytical approach. The accuracy due to physical errors may not be high, but the time of computation is very short and it is easy to prepare and implement the input data set.

The main program consists of the input data file, electromagnetic module, structural module (natural frequencies of the stator system), and acoustic module (Fig. 2a). The following effects can be included: phase current unbalance, higher space harmonics, higher time harmonics, slot openings, slot skew, rotor static eccentricity, rotor dynamic eccentricity, armature reaction, magnetic saturation. An auxiliary program calculates the torque ripple [10], converts the tangential magnetic forces into equivalent radial forces, and transfers radial forces due to the torque ripple to the main program.

The input data file contains the dimensions of the machine and its stator and rotor magnetic circuit, currents (including unbalanced system and higher time harmonics), winding parameters [2], material parameters (specific mass, Young modulus, Poisson's ratio), speed, static and dynamic eccentricity, skew, damping factor as a function of frequency, correction factors; e.g., for the stator systems natural frequencies, maximum force order taken into consideration, minimum threshold magnetic flux density to exclude all magnetic flux density harmonics below the selected margin. The rotor magnetic flux density waveforms are calculated on the basis of MMF waveforms and per-

<sup>1</sup> industry standard technical calculation tool for professionals, educators, and college students

<sup>2</sup> fully integrated technical computing environment used by scientists, engineers, analysts, educators, and college students

meances of the air gap. Magnetic forces are calculated on the basis of Maxwell stress tensor. The natural frequencies of the stator system can be approximately evaluated as [9]:

$$f_{mm} \approx \frac{1}{2\pi} \sqrt{\frac{K_m^{(c)} + K_m^{(f)} + K_m^{(w)}}{M_c + M_f + M_w}}, \quad (4)$$

where  $K_m^{(c)}$  is the lumped stiffness of the stator core for the  $m$ th circumferential vibrational mode,  $K_m^{(f)}$  is the lumped stiffness of the frame for the  $m$ th circumferential and  $n$ th axial vibrational mode,  $K_m^{(w)}$  is the lumped stiffness of the stator winding for the  $m$ th circumferential vibrational mode,  $M_c$  is the lumped mass of the stator core,  $M_f$  is the lumped mass of the frame, and  $M_w$  is the lumped mass of the stator winding. It has been assumed the frame is a circular cylindrical shell with both ends constrained mechanically by end bells.

These values can be corrected with the aid of correction factors obtained, e.g., from the FEM structural package or measurements. Then, using the damping coefficient  $\zeta_m$  which is a function of frequency and radial forces  $F_{mr}$ , the amplitudes of radial velocities for the  $m$ th circumferential mode are calculated, i.e.

$$A_{mr} = \frac{F_{mr}/[(2\pi f_m)^2 M]}{\sqrt{[1 - (f_r/f_m)^2]^2 + [2\zeta_m (f_r/f_m)]^2}}. \quad (5)$$

The damping factor  $\zeta_m$  affects significantly the accuracy of computation. Detailed research has shown that the damping factor is a nonlinear function of natural frequencies  $f_m$ . The radiation efficiency factor  $\sigma_m$ , acoustic impedance  $Z_0$  of the air and radial velocities  $v_m$  give the SWL radiated by the  $m$ th mode of the machine structure, i.e.

$$\Pi_m = \sigma_m Z_0 S_f v_m^2, \quad (6)$$

where  $Z_0 = \rho_0 c_0$ ,  $\rho_0 = 1.188 \text{ kg/m}^3$  is the air density,  $c_0 = 344 \text{ m/s}$  is the sound velocity in the air,  $S_f$  is the surface of the motor frame and  $v_m = 2\pi f_r A_{mr}$  is the spatial averaged mean square velocity of the  $m$ th circumferential mode. After performing calculations of SWL for every frequency  $f_{rk}$ , where  $k = 1, 2, 3, \dots$ , present in the excitation force spectrum, the SWL spectrum (narrow band noise) can be found. If  $\Pi_{mk}$  is the amplitude of the SWL for the  $k$ th harmonic  $1 \leq k \leq k_{\max}$ , the overall noise can be found as

$$\Pi = \sqrt{\sum_{k=1}^{k_{\max}} \Pi_{mk}^2} \quad (7)$$

The overall SWL calculated in such a way is lower than that obtained from measurements, because computations include only the noise of magnetic origin (mechanical noise caused by bearings, shaft misalignment, and fan is not taken into account) and usually, the calculation is done for low number of harmonics of magnetic flux density waves.

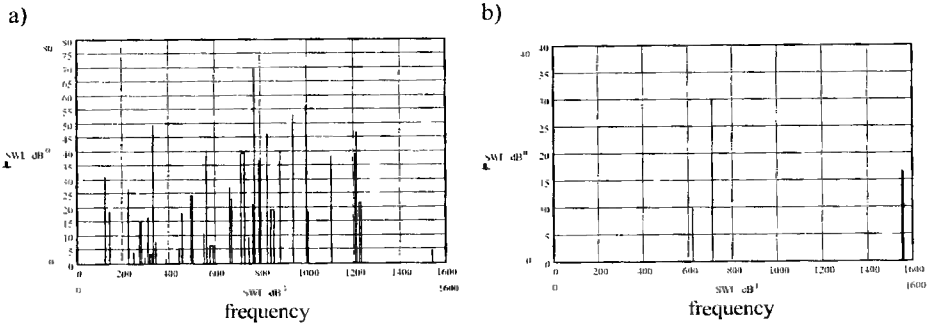


Fig. 3. SWL spectrum of 10-kW, 660-rpm,  $s_l = 36$ -slot PM brushless motors at  $\psi \vartheta = 4.58^\circ$ : (a)  $2p = 10$ , stator current frequency  $f = 55$  Hz, overall SWL = 70.32 dB; (b)  $2p = 8$ ,  $f = 44$  Hz, overall SWL = 29.95 dB.

The proper selection of the stator slots  $s_l$  and rotor poles  $2p$  is one of the primary factors affecting the noise of magnetic origin of PM brushless motor. For a motor with  $s_l = 36$  slots and  $2p = 10$  poles the overall SWL at 660 rpm is 70.32 dB or  $1.08 \times 10^{-5}$  W. The SWL spectrum is shown in Fig. 3a. All fundamental frequencies, circumferential modes and SWL obtained from calculations and measurements are listed in Table 2.

Table 2. Calculated key frequencies and modes of SWL at  $\psi \vartheta \psi = 4.58^\circ$  (frequencies producing noise below 25 dB have been neglected).

SWL, dB		SWL frequency, Hz	SWL frequency equation	mode (order)
calculation	test			
30.8	36.98	121	$(2k + 1/p)f, k = 1$	2
26.5	44.38	220	$2kf, k = 2$	2
49.14	50.10	330	$2kf, k = 3$	2
24.23	41.14	495	$(2k + 1)f, k = 4$	2
39.84	28.30	561	$(2k + 1/p)f, k = 5$	2
26.67	43.80	660	$2kf, k = 6$	2
22.77	36.84	671	$(2k + 1/p)f, k = 6$	2
39.14	46.26	715	$(2k + 1)f, k = 6$	2
20.85	38.09	759	$(2k - 1/p)f, k = 7$	2
<b>69.69</b>	<b>68.10</b>	<b>770</b>	$2kf, k = 7$	<b>2</b>
36.46	39.78	781	$(2k + 1/p), k = 7$	2
37.16	34.23	792	$2(k + 1/p), k = 7$	2
45.92	39.20	825	$(2k + 1)f, k = 7$	2
39.88	55.42	880	$2kf, k = 8$	2
56.02	52.24	990	$2kf, k = 9$	2
38.06	43.80	1100	$2kf, k = 10$	2
38.9	40.69	1199	$(2k - 1/p)f, k = 11$	2
46.64	40.60	1210	$2kf, k = 11$	2
70.32	68.73	Overall SWL		

The predominant amplitude of the SWL = 69.69 dB (calculations) for  $r = 2$  is at  $f_r = 2 \times 7 \times 55 = 770$  Hz [9]. This force is produced by interaction of the PM rotor field and slotted structure of the stator [9]. The frequency of this force is  $f_r = 2\mu_\lambda f$  and

order  $r = 2|\mu_\lambda p - s_1|$ , where  $\mu_\lambda = \text{int}\left(\frac{s_1}{p}\right)\mu_\lambda$ . If the frequency of this force is close to the natural frequency of the order  $r = m = 2$ , a large amplitude of the SWL is produced. In the investigated motor the natural frequency  $f_{m=2, n=1} = 1044$  Hz and the effect of interaction of the PM rotor field on the stator slotted structure ( $f_r = 770$  Hz) is still significant.

If the number of stator slots  $s_1 = 36$  remains the same and  $2p = 8$ , the overall SWL at 660 rpm is reduced to 30 dB ( $10^{-9}$  W). The SWL spectrum is shown in Fig. 3b. The predominant amplitude of the SWL = 29.94 dB at  $f_r = 2 \times 8 \times 44 = 704$  Hz ( $\mu_\lambda = 8$ ). The amplitude of noise is much smaller than that for  $2p = 10$  because the radial force order  $r = |\mu_\lambda p - s_1| = |8 \times 4 - 36| = 4$  is greater than in the previous case [13]. The natural frequency  $f_{m=4, n=1} = 2938$  Hz is much higher than  $f_r$ , too. The other amplitudes, i.e., 9.55 dB at  $f_r = 2 \times 7 \times 44 = 616$  Hz ( $k = 7$ ) and 16.43 dB at:

$$f_r = (2k + 1 + 1/p)f = (2 \times 17 + 1 + 1/4)44 = 1551 \text{ Hz } (k = 17)$$

are also due to magnetic forces of the order  $r = 4$  (Fig. 3b).

On the other hand, the 10-pole motor produces lower cogging torque than the 8-pole motor because the least common factor LCM of the number of slots  $s_1$  and poles  $2p$  is greater for the 10-pole motor, i.e.,  $\text{LCM}(36, 8) = 72$ ,  $\text{LCM}(36, 10) = 180$  [8].

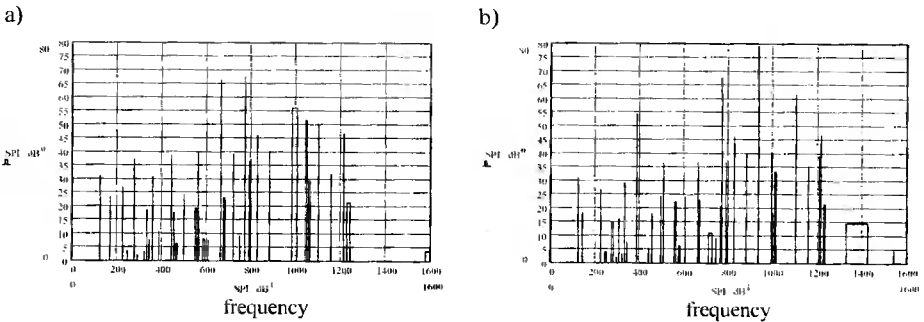


Fig. 4. SWL spectrum of a 10-kW, 660-rpm,  $2p = 10$ ,  $s_1 = 36$ -slot PM brushless motors at: (a) angle  $\psi \psi \delta = 5^\circ$  between the stator current and  $q$ -axis; (b)  $\psi \psi \delta \psi = 4.5^\circ$

When the rotational speed increases, the SWL usually increases too. However, this rule is not always true, because while the speed increases the frequencies of low order radial magnetic forces may not match the corresponding natural frequencies of the stator-frame system.

The SWL spectrum of a PM brushless motor is very sensitive to the angle  $\psi \delta$  between the stator current phasor and the  $q$ -axis (EMF phasor). Fig. 4 shows how the SWL spectrum is changed, if the angle  $\psi \delta \psi$  increases from  $4.58^\circ$  to  $5^\circ$  (see also Fig. 3a) and then decreases to  $4.5^\circ$ .

## 6. ACCURACY OF NOISE PREDICTION

The results of both analytical and numerical noise prediction may considerably differ from measurements (Fig. 5). Forces that generate vibration and noise are only a small

fraction of the main force produced by the interaction of the fundamental current and the fundamental normal component of the magnetic flux density. Approximately only  $10^{-10}$  to  $10^{-6}$  of the electrical input power of a 10 kW motor is converted into acoustic power.

The accuracy of the predicted SWL spectrum depends not only how accurate the model is, but also how accurate the input data are, e.g., level of current unbalance, angle  $\psi$  between the stator current and  $q$ -axis (Fig. 4), influence of magnetic saturation on the equivalent slot opening, damping factor, elasticity modulus of the slot content (conductors, insulation, encapsulation), higher time harmonics of the input current (inverter-fed motor), etc. All the above input data are difficult to obtain or predict with sufficient accuracy [7, 16].

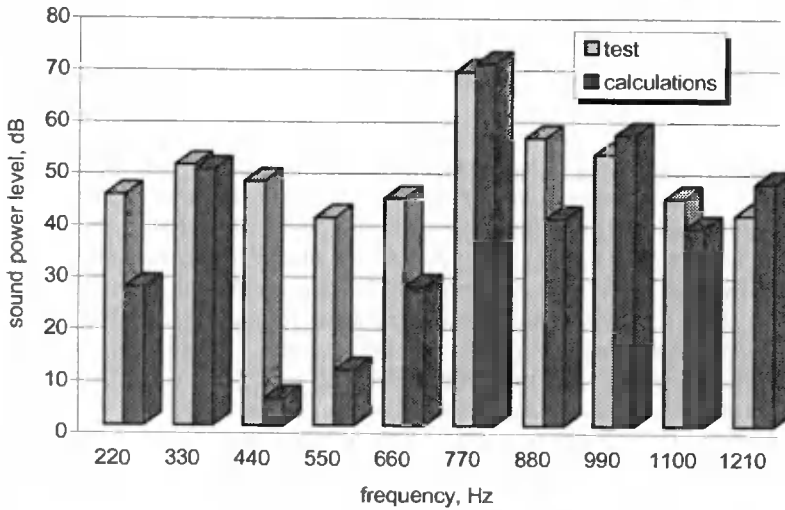


Fig. 5. Comparison of analytically predicted SWL amplitudes with those obtained from measurements for key radial force frequencies  $4f$ ,  $6f$ ,  $8f$ ,...  $12f$  of the order  $r = 2$  for a 10 kW,  $2p = 10$ ,  $s_l = 36$ ,  $f = 55$  Hz,  $\psi \vartheta = 4.58^\circ$  PM brushless motor.

## 7. CONCLUSIONS

The accurate prediction of the noise of a PM brushless motor at the early stage of design is much more difficult than electromagnetic, thermal or structural calculations.

Analytical methods of noise prediction of PM brushless motors may be preferred to numerical methods in design calculations, even if their accuracy is not high. The main advantage of analytical methods is easy preparation of the input data file and fast time of computations (seconds, maximum a few minutes).

The most difficult problem in analytical prediction of noise is the accurate calculation of natural frequencies of the stator core-winding-frame system.

The proper selection of the number of stator slots with respect to the number of rotor poles is very important to design a low-noise PM synchronous motor. On the other hand, a low-noise PM synchronous motor may produce a high cogging torque.

The order  $r$  (circumferential mode  $m$ ) of radial magnetic forces increases with the number of poles  $2p$ . The larger the magnetic force order, the lower the deflection of the stator core which is inversely proportional to the 4<sup>th</sup> power of the force order [9].

The calculated noise level is usually lower than that obtained from laboratory measurements because calculations may not include all harmonic forces [16].

## BIBLIOGRAPHY

- [1] Jordan H., 1951: *Der Geräuscharme Elektromotoren*, Verlag W. Girardet, Essen.
- [2] Yang S.J., 1981: *Low-noise electrical motors*, Clarendon Press, Oxford.
- [3] Timar P.L., Fazekas A., Kiss J., Miklos A., Yang S.J., 1989: *Noise and vibration of electrical machines*, Elsevier, Amsterdam – Oxford – New York – Tokyo.
- [4] Kwasnicki S., 1998: *Magnetic noise of cage induction motors* (in Polish), BOBRME Komel, Katowice.
- [5] Heller B., Hamata V.: *Harmonic field effects in induction machines*, Academia (Czechoslovak Academy of Sciences), Prague, Italy.
- [6] Witczak P., 1995: *Determination of mechanical vibration caused by magnetic forces in induction machines* (in Polish), Politechnika Lodzka, Zesz. Nauk. No 725, Lodz.
- [7] Verdyck D., Belmans R.J.M., 1994: *An acoustic model for a permanent magnet machine: modal shapes and magnetic forces*, IEEE Trans. on IA, Vol. 30, No. 6, 1625-1631.
- [8] Zhu Z.Q., Howe D., 1993: *Electromagnetic noise radiated by brushless permanent magnet d.c. drives*, Electr. Machines and Drives Conf., Oxford, U.K., 606-611.
- [9] Gieras J.F., Wang C., Lai J.C., 2005: *Noise of polyphase electric motors*, CRC Press – Taylor & Francis, Boca Raton – London – New York.
- [10] Gieras J.F., 2004: *Analytical approach to cogging torque calculation of PM brushless motors*, IEEE Trans. on IA, 34, No 5, 1310-1316.
- [11] Wang C., Lai J.C.S., 2000: *Prediction of natural frequencies of finite length cylindrical shells*, Appl. Acoustics, 59, No. 4, 431-447.
- [12] Wang C., Lai J.C.S., Pulle D.W.J., 1999: *A statistical method for the prediction of acoustic noise radiation from induction motors*, European Power Electronics Conf. EPE'99, Lausanne, Switzerland, Vol. 8, 1-8.
- [13] Wang C., Lai J.C.S., Pulle D.W.J., 2002: *Prediction of acoustic noise from variable-speed induction motors: Deterministic versus statistical approaches*, IEEE Trans. on IA, 38, No. 4, 1037-1044.
- [14] Lyon R.H., 1975: *Statistical energy analysis of dynamical systems: theory and applications*, MIT Press, Cambridge, MA, USA.
- [15] Delaree K., Iadevaia M., Heylen W., Saa P., Hameyer H., Belmans R., 1999: *Statistical energy analysis of acoustic noise vibration for electric motors: transmission from air gap field to motor frame*, IEEE IAS 1999 Conf. and Meeting, 1897-1902.
- [16] Walker J.H., Kerruish N., 1960: *Open-circuit noise in synchronous machines*, Proc. IEE, Part A, 107, No. 36, 505-512.

## OBLICZENIA ANALITYCZNE HAŁASU AKUSTYCZNEGO WYWOŁANEGO POLEM MAGNETYCZNYM W SILNIKACH BEZSZCZOTKOWYCH O MAGNESACH TRWAŁYCH

### Streszczenie

Obliczenia hałasu akustycznego generowanego przez silniki elektryczne są obecnie ważnym zagadnieniem zarówno dla producentów jak i użytkowników maszyn elektrycznych. W artykule przedstawiono podejście inżynierskie do obliczeń hałasu wywołanego polem magnetycznym w silnikach bezszczotkowych o magnesach trwałych. Poziom mocy akustycznej (PMA) jest obliczany na podstawie analizy pola magnetycznego w szczelinie powietrznej, sił promieniowych, częstotliwości naturalnych układu stojan-obudowa oraz współczynnika wypromieniowania dźwięku. Przedmiotem dyskusji są zagadnienia dokładności obliczeń na podstawie metod analitycznych oraz numerycznych.

Słowa kluczowe: magnesy trwałe, silniki bezszczotkowe, hałas, pole magnetyczne





## ELECTROMECHANICAL PORTABLE ENERGY HARVESTING DEVICE: ANALYSIS AND EXPERIMENTAL TESTS

Jacek F. Gieras<sup>\*</sup>, Jae-Hyuk Oh<sup>\*\*</sup>, Mihai Huzmezan<sup>\*\*</sup>

<sup>\*</sup>University of Technology and Life Sciences  
Al. S. Kaliskiego 7, 85-796 Bydgoszcz, Poland, e-mail: jgieras@ieee.org

<sup>\*\*</sup>United Technologies Research Center  
411 Silver Lane, East Hartford, CT 06108, USA

*Summary:* This paper presents the design analysis and performance of an energy harvesting prototype device operating on the principle of electromechanical energy conversion. The input vibration kinetic energy is converted into the output electrical energy. A spring – mass system with moving permanent magnet (PM) is mechanically excited by external vibrations. The voltage is induced in a stationary coil that is embraced by PM poles. When the coil is loaded with an external impedance, an electric current proportional to the induced EMF arises in the external circuit. Fundamental equations for performance calculations have been derived on the basis of elementary beam theory and circuit analysis. A prototype has been built and the calculation results have been validated with the test results.

Keywords: energy harvesting, vibration generator, electromechanical, permanent magnets

### 1. INTRODUCTION

Self-powered microsystems have recently been considered as a new area of technology development. Interest in self-powered microsystems have been previously addressed in several papers, e.g. [1,6-10]. Main reasons, which stimulate research in this new area are:

- large numbers of distributed sensors,
- sensors located in positions where it is difficult to wire or charge batteries,
- reduction in cost of power and communication,
- Moore's law (the number of transistors per unit area of an IC doubles every 18 months).

Microsystems can be powered by energy harvested from a range of sources present in the environment. Solar cells, thermoelectric generators, kinetic generators, radio power, leakage magnetic or electric fields are just a few examples. In some applications, e.g., container security systems, condition monitoring of machine parts (motors, turbines, pumps, gearboxes), permanent embedding in inaccessible structures (bridges,

roads, towers, masts), or animal tracking, the only source of electrical energy is the kinetic energy.

The harvesting of kinetic energy is the generation of electrical power from the kinetic energy present in the environment. The nature of the kinetic energy harvesting mechanism in a *self contained system* depends upon the nature of the application [6,7,11]. Kinetic energy harvesting devices can be divided into two groups:

- acceleration/vibration and spring mass system devices, e.g. kinetic watches (*Asulub, Seiko*), cantilever beam vibration generators, moving magnet linear generators [1,2,3,6,7,9,12];
- repeated straining physical deformation devices, e.g. piezoelectric generators or magnetic shape memory generators [8,10,11].

This paper discusses a portable electromechanical energy harvesting device with the magnetic field excitation system integrated with the cantilever beam (i.e. flat spring) and a stationary multiturn coil. The maximum generated energy is when the mechanical resonance occurs, i.e. when the natural frequency of the cantilever beam-based vibrating system is the same or close to the input frequency of vibration. Potential applications include: (1) wireless sensors installed in security systems of containers or trailers, (2) condition-based monitoring of machinery and structures; (3) implanted medical sensors; (4) wearable computers; (5) intelligent environments (“smart space”), etc. The solution designed and presented here is down scalable to the MEMS levels; however, micro-collisions, air friction dissipation, and cushioning effects cannot be ignored.

## 2. FUNDAMENTAL EQUATIONS

A small cantilever beam (spring) with permanent magnets (PMs) fixed to one tip is an integral part of the electromechanical energy harvesting device (Fig. 1). High energy moving PMs induce the EMF in the stationary flat coil. The EMF gives a rise to electric current in an external circuit.

As it is known, the moment of area (inertia)  $I_a$  and stiffness  $k$  of a cantilever (clamped-free) beam are, respectively,

$$I_a = \frac{1}{12} wt^3 \quad \text{and} \quad k = \frac{3EI_a}{L^3} \quad (1)$$

where  $w$  is the width of the cantilever beam (flat spring),  $t < w$  is its thickness,  $L$  is its length, and  $E$  is the Young’s modulus (elasticity modulus). Consequently, the natural angular frequency of a cantilever beam for the  $n$ -th *mode shape* or characteristic deflection shape is expressed as

$$\omega_{\text{nat}} = \sqrt{\frac{k}{m}} = \sqrt{\frac{3EI_a}{mL^3}} = a_n \sqrt{\frac{EI_a}{m_b L^3}} \quad (2)$$

Thus, the natural frequency  $f_{\text{nat}} = \omega_{\text{nat}}/(2\pi)$  for the  $n$ -th mode shape of a cantilever beam can simply be controlled by changing the length  $L$  of the beam.

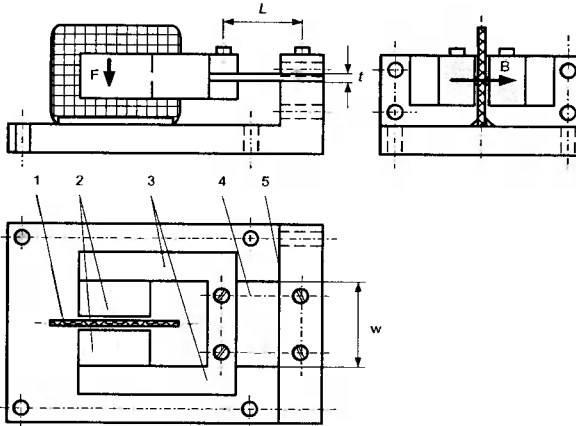


Fig. 1. Principle of operation of the proposed electromechanical energy harvesting device: 1 – stationary coil, 2 – NdFeB PMs, 3 – mild steel magnetic circuit, 4 – cantilever beam (flat spring), 5 – base.

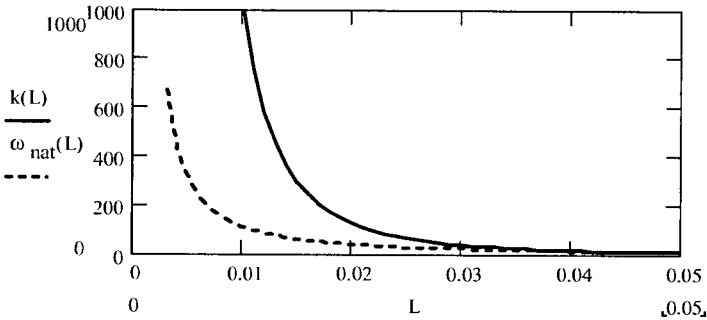


Fig. 2. Spring constant  $k$  (N/m) and natural frequency  $\omega_{nat}$  (1/s) as functions of the length  $L$  of a steel cantilever beam of the tested energy harvesting device ( $w = 19.15$  mm,  $t = 0.1$  mm,  $E = 210\,000$  N/m)

In elementary beam theory the vibration of a cantilever beam is replaced by a spring-mass system model, as shown in Appendix I. Therefore, the modal mass  $m$  in eqn (2) is not equal to the mass  $m_b$  of the cantilever beam. For the  $n = 1$  mode shape the modal mass is [5]

$$m = 0.2357m_b \tag{3}$$

and the coefficient  $a_n = 3.52$  (see Appendix I).

The operation of an electromechanical energy harvesting device requires a concentrated mass  $M$  that is fixed to the tip. This mass represents the mass of PMs and mild steel magnetic circuit. The total modal mass is

$$m = 0.2357m_b + M \approx M \tag{4}$$

because  $m_b \ll M$ . In the investigated prototype the mass of beam  $m_b = 0.00015$  kg while the mass of the PM excitation system  $M = 0.083$  kg. Thus, for an energy harvesting device the predominant shape mode  $n = 1$  and natural angular frequency

$$\omega_{nat} = \sqrt{\frac{3EI_a}{(0.2357m_b + M)L^3}} \approx \frac{1}{2} \sqrt{\frac{Ewt^3}{ML^3}} \quad (5)$$

The spring constant  $k$  and natural frequency  $\omega_{nat}$  versus the length  $L$  of cantilever beam used in the tested energy harvesting device are plotted in Fig. 2.

For a spring – mass system with damper, the cantilever beam with PMs under the effect of *forced motion* will become a single-degree-of-freedom vibrating system that can be described by

$$m\ddot{x}(t) + c\dot{x}(t) + kx(t) = F_m \sin(\omega t) \quad (6)$$

where  $F_m \sin(\omega t)$  is an external force with the amplitude  $F_m$  considered for simplicity as changing sinusoidally with the time  $t$  and  $c$  is the coefficient of a viscous damping. The external force  $F_m \sin(\omega t)$  can be produced by a vibrating body on which the cantilever beam with PM is placed. The solution to eqn (6) can be written as

$$x(t) = \sqrt{A^2 + B^2} \sin(\omega t + \phi) = X_m \sin(\omega t + \phi) \quad (7)$$

$$\tan \phi = \frac{B}{A} \quad (8)$$

The transfer function and time response are given in Appendix II. By examining eqn (6) it becomes apparent that the energy of vibration is converted into electrical energy with maximum efficiency if the frequency  $\omega$  the external source of vibration is close to the natural frequency  $\omega_{nat}$  of the spring-mass system. After solving eqn (6), the forced vibration amplitude  $X_m$  (with applied force) and magnification factor  $MF$  can be expressed as

$$X_m = \frac{\frac{F_m}{k}}{\sqrt{\left[1 - \left(\frac{\omega}{\omega_{nat}}\right)^2\right]^2 + \left(2\zeta \frac{\omega}{\omega_{nat}}\right)^2}}; \quad MF = \frac{X_m}{\frac{F_m}{k}} \quad (9)$$

where  $\zeta = c/c_c$  is the damping coefficient and  $c_c = 2m\omega_{nat}$  is the critical damping coefficient. Both  $X_m$  and  $MF$  take maximum values for low damping coefficient  $\zeta$  and frequency of vibration  $f_n = \omega_n/(2\pi)$  equal to or very close to  $f_{nat} = \omega_{nat}/(2\pi)$ . Fig. 3 shows the magnification factor  $MF$  according to eqn (13) for three values of damping coefficients  $\zeta = 0.1, 0.2,$  and  $0.3$ .

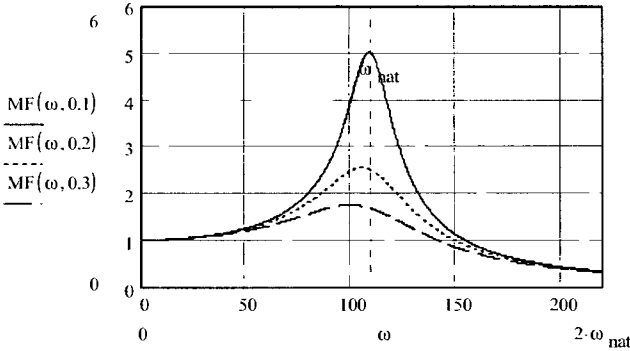


Fig. 3. Damping coefficient  $MF$  according to eqn (9) as a function of angular frequency  $\omega$  for three values of damping coefficients  $\zeta = 0.1, 0.2,$  and  $0.3$ .

### 3. OUTPUT POWER

To generate electrical energy, a stationary coil is placed between the poles of vibrating PMs. The instantaneous voltage induced (or EMF) in a single turn (two conductors)  $e(t) = 2 B l_M v(x)$  where  $B$  is the average magnetic flux density produced by PMs and  $l_M$  is the length of the PM (measured along the coil). According to eqn (7), the linear velocity  $v(t) = dx(t)/dt = 2\pi f X_m \cos(\omega t + \phi)$ . For  $N$  turns the EMF is  $e(t) = 4\pi f N B l_M X_m \cos(\omega t + \phi)$ . The peak value of the EMF is  $E_m = 4\pi f N B l_M X_m$  and the *rms* value

$$E = 2\sqrt{2}\pi f N B l_M X_m = 2\sqrt{2}\pi\alpha_i f N B_m l_M X_m, \quad (10)$$

where the average-to-peak value ratio of the magnetic flux density can be approximately found as

$$\alpha_i = \frac{B}{B_m} \approx \frac{l_M}{l_M + 2g}. \quad (11)$$

Similarly, the electromagnetic reaction force produced by the PM excitation field  $B$  and current in the coil  $I$  is

$$F_{elm} = \sqrt{2}\alpha_i B_m N I l_M. \quad (12)$$

Eqn (12) has been found assuming that the phase angle between the EMF  $E$  and current  $I$  is zero, i.e.  $EI = F_{elm} v$ . The electromagnetic force  $F_{elm}$  is very small because the current in the coil is low, e.g., for the tested prototype and  $N = 300$  turns  $F_{elm} = 0.015$  N when  $I = 0.01$  A and  $F_{elm} = 0.107$  N when  $I = 0.07$  A.

Although theoretically justified, equations derived in [12], not always give the expected results.

If a load impedance  $Z_L = R_L + jX_L$  is connected across the coil terminals, a closed electrical circuit will be created. The *rms* current  $I$  in the circuit and *rms* voltage  $V$  across the load impedance  $Z_L$  are, respectively,

$$I = \frac{E}{\sqrt{(R_c + R_L)^2 + (X_c + X_L)^2}} \approx \frac{E}{R_c + R_L} \quad (13)$$

$$V = I\sqrt{R_L^2 + X_L^2} \quad (14)$$

where  $Z_c = R_c + jX_c$  is the internal impedance of the coil. Since the coil is not furnished with any ferromagnetic core and the vibration frequency is low (usually less than 30 Hz), Hz),  $R_c \gg X_L$ . For resistive load the load inductance  $X_L$  can also be neglected. The output active power of the device can simply be found as:

$$P_{out} = I^2 R_L \quad (15)$$

where  $R_L$  is the load resistance. Further, the current  $I$  can be rectified and used for charging a battery, which in turn energizes an electronic device, e.g., a wireless sensing system [7,12].

The maximum output power is at resonance, i.e.  $\omega = \omega_{nat}$ . Combining together eqns (2), (9), (10), (13) and (15), assuming  $R_c \gg X_c$ , and neglecting the load inductance  $X_L$ , the maximum output power is

$$P_{max} \approx \frac{\alpha_c^2}{2\zeta^2} \left( \frac{NB_m I_M F_m}{\omega_{nat} M} \right)^2 \frac{1}{R_c^2 / R_L + 2R_c + R_L} \quad (16a)$$

For  $R_L = R_c$  eqn (16a) takes simpler form, i.e.,

$$P_{max} \approx \frac{\alpha_c^2}{\zeta^2} \left( \frac{NB_m I_M F_m}{\omega_{nat} M} \right)^2 \frac{1}{8R_c} \quad (16b)$$

The output power of an electromechanical device with cantilever beam is high when:

- the damping  $\zeta$ , natural frequency  $\omega_{nat}$ , tip mass  $M$ , and coil resistance  $R_c$  are low;
- the number of turns  $N$ , magnetic flux density  $B$ , length of magnets  $I_M$ , and amplitude of external force  $F_m$  are as high as possible.

High magnetic flux density  $B$  in the air gap can be maintained if high energy PMs are used and the gap between PM poles is small. Fig. 4 shows the maximum power at resonance ( $f_{nat} = 17.1$  Hz) generated by the investigated energy harvesting device as a function of the damping  $\zeta$  coefficient. Even for very low damping coefficient  $\zeta = 0.05$  the maximum output power does not exceed 65 mW.

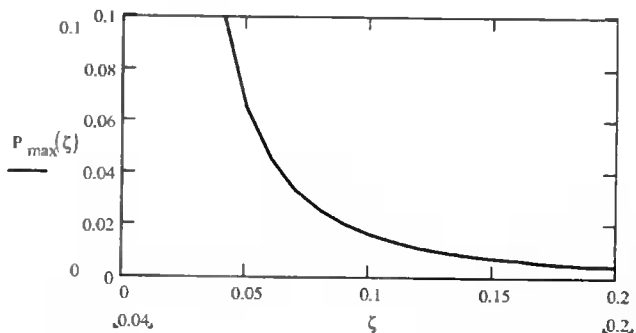


Fig 4. Maximum output power (W) generated by the investigated energy harvesting device at resonant versus damping  $\zeta$  coefficient  $\zeta$  for  $f_{nat} = 17.1$  Hz,  $N = 200$ ,  $B = 0.85$  T,  $l_M = 11$  mm,  $F_m = M \cdot g = 0.819$  N,  $M = 0.083$  kg,  $R_c = 6.93$   $\Omega$ , and  $R_L = 4.7$   $\Omega$ .

#### 4. PROTOTYPE

On the basis of eqns (1) to (16) a prototype of a small energy harvesting electro-mechanical device (Fig. 5) has been designed and built for research purposes. Specifications are given in Table I. As a cantilever beam (flat spring) both steel and beryllium copper ribbons have been used. The natural frequency of the spring – mass system can be adjusted either by changing the length  $L$  of the cantilever beam or adding more than one spring in parallel. The stationary coil has been wound with round copper wire. The coil has three taps (100+100+100) and the total number of turns  $N = 300$ .

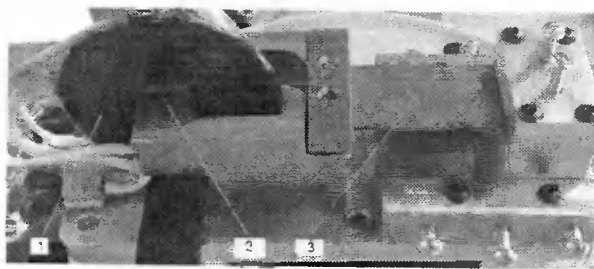


Fig. 5. Prototype of the energy harvesting electromechanical device: 1 – coil, 2 – PM, 3 – cantilever beam.



Table 1. Specifications of energy harvesting electromechanical device.

Dimensions of a single PM	$l_M = w_M = 11$ mm, $h_M = 8$ mm
Material of PMs	Sintered NdFeB, $B_r = 1.3$ T
Number of poles	2
Number of turns (tapped winding)	100 + 100 + 100 (max. 300)
Wire diameter	0.255 mm (AWG 30)
Air gap between PMs	4 mm
Mass of vibrating system with PMs (tip mass)	0.083 kg
Mass of cantilever beam per length	0.015 kg/m
Thickness of cantilever beam	0.10 mm
Width of cantilever beam	19.15 mm
Length of cantilever beam	Adjustable from 5 to 45 mm
Natural frequency	Adjustable from 8 to 30 Hz
Material of flat spring	Steel (alternatively beryllium copper)
Coil thickness	2 mm
Coil resistance (200 turns)	6.93 $\Omega$
Coil resistance (300 turns)	10.27 $\Omega$
Coil inductance (200 turns)	13.2 $\mu$ H
Coil inductance (300 turns)	29.8 $\mu$ H
Damping factor $\zeta$	Approximately 0.1
Measured maximum output power	10 to 18 mW

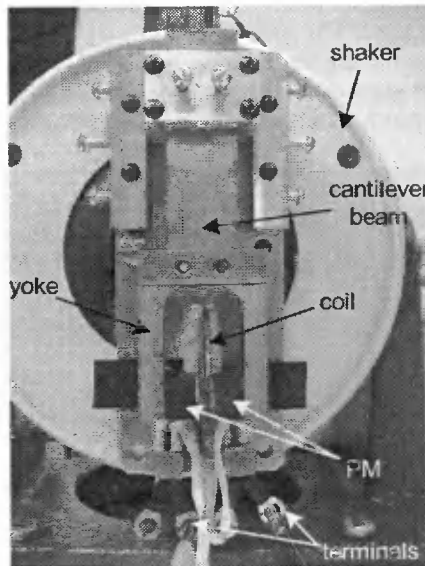


Fig. 6. Prototype of the energy harvesting electromechanical device placed on a small variable-frequency shaker

The device has been tested on a small shaker to provide a variable-frequency, variable-amplitude vibration. The electrical quantities have been measured using a multi channel oscilloscope. The acceleration of the shaker has been measured using a piezoelectric accelerometer. The energy harvesting device placed on the shaker is shown in Fig. 6.

## 5. MAGNETIC CIRCUIT

The magnetic circuit consists of two rectangular sintered NdFeB PMs and mild steel U – shaped yoke. The dimensions of PMs are as follows: axial length (along cantilever beam)  $l_M = 11$  mm, width (perpendicular to the base)  $w_M = 11$  mm, and height (parallel to the main magnetic flux)  $h_M = 8$  mm.

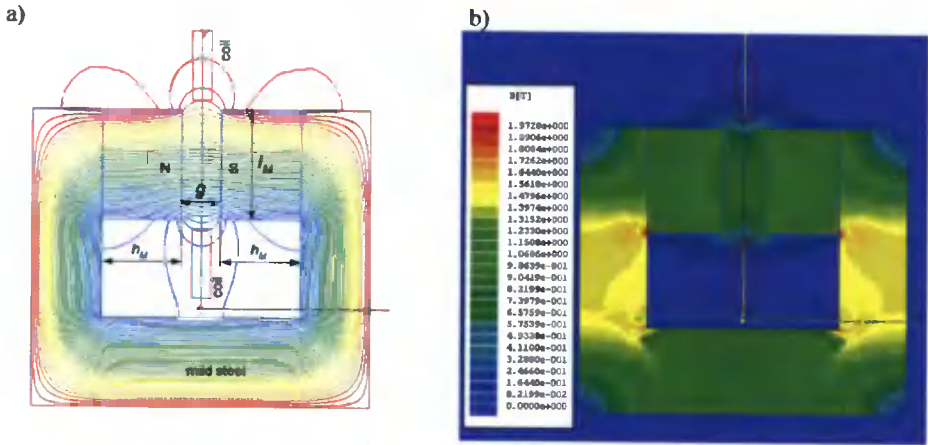


Fig. 7. Resultant magnetic field distribution excited by PMs and coil current (300 turns, 0.07 A): (a) magnetic flux lines; (b) magnetic flux density distribution. 2D FEM simulation.

The resultant 2D magnetic field distribution excited both by PMs and coil current as obtained from the FEM is shown in Fig. 7. The distribution of magnetic flux density excited by the coil alone ( $N = 300$ ,  $I = 0.07$  A) is shown in Fig. 8. The distribution of normal and tangential components of the magnetic flux density in the center line of the air gap excited by PMs is shown in Fig. 9. The distribution of normal and tangential components of the magnetic flux density along the center line of the air gap excited by the coil current (300 turns, 0.07 A) is shown in Fig. 10. Figs. 7 to 10 have been obtained using commercial 2D *Maxwell Ansoft* FEM software.

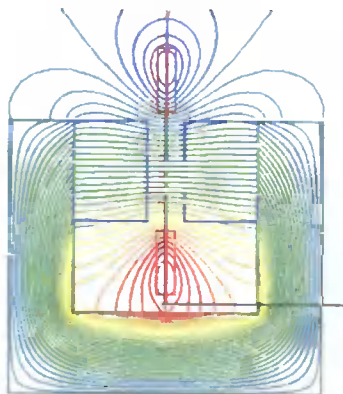


Fig. 8. Magnetic flux distribution excited by the coil with 300 turns and 0.07 A current. 2D FEM simulation.

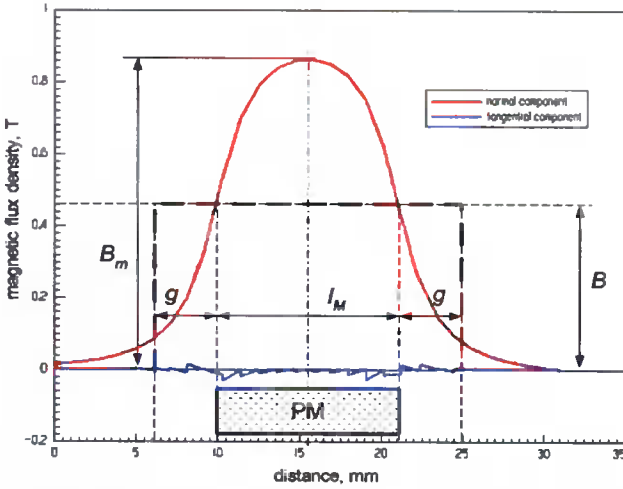


Fig. 9. Normal and tangential component distributions of the magnetic flux density excited by NdFeB PMs at zero coil current along the center line of the air gap (Tesla vs mm). 2D FEM simulation.

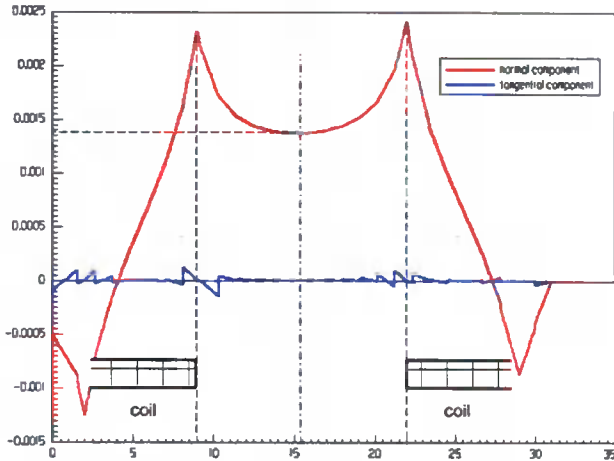


Fig. 10. Normal and tangential component distributions of the magnetic flux density excited by the coil current 0.07 A (300 turns) along the center line of the air gap (Tesla vs mm) assuming that PMs are removed. 2D FEM simulation.

Even for very high coil current (normally, a current lower than 0.07 A is induced), the normal component of the magnetic flux density excited by the coil MMF is negligible as compared with the magnetic flux density excited by PMs. For the center of the coil – magnet system, the normal component of the magnetic flux density excited by the coil is only 0.015 T while the magnetic flux density excited by PMs is 0.86 T. Thus the reaction of the coil currents can be neglected in calculation of the PM vibration generator. Also, the electromagnetic reaction force produced by the PM excitation field and coil current is small – eqn (12).

Similar value of the air gap magnetic flux density can be obtained analytically, i.e.:

$$B_m \approx \frac{B_r}{1 + \mu_{rec} g' h_M}, \quad (17)$$

where  $B_r$  is the remanent magnetic flux density,  $\mu_{rec}$  is the relative recoil magnetic permeability,  $g$  is the air gap (magnet-to-magnet), and  $h_M$  is the PM height per pole. For the tested prototype  $B_r = 1.3$  T,  $\mu_{rec} = 1.089$ ,  $g = 4$  mm, and  $h_M = 8$  mm that gives  $B_m = 0.842$  T. From Kirchoff's equation for the magnetic voltage

$$2 \frac{B_r}{\mu_o \mu_{rec}} h_M = 2 \frac{B_m}{\mu_o} \left( \frac{h_M}{\mu_{rec}} + g k_{sat} \right), \quad (18)$$

where the saturation factor of the magnetic circuit

$$k_{sat} = 1 + \frac{\sum H_{F_{el}} l_{F_{el}}}{2 B_m g' \mu_o} \geq 1. \quad (19)$$

In the above eqn (19)  $\sum H_{F_{el}} l_{F_{el}}$  is the magnetic voltage drop in the mild steel portions of the magnetic circuit,  $H_{F_{el}}$  is the magnetic field intensity in the  $i^{\text{th}}$  portion of the magnetic circuit, and  $l_{F_{el}}$  is the length of the  $i^{\text{th}}$  portion of the magnetic circuit. The saturation factor of the tested prototype is very close to unity (unsaturated magnetic circuit) because the air gap is large ( $g = 4$  mm).

## 6. COMPARISON OF CALCULATIONS WITH TEST RESULT

Fig. 11 shows a comparison of the output (terminal) voltage and Fig. 12 shows the comparison of the *rms* current and output power obtained from calculations and measurements. The natural frequency of the cantilever beam has been adjusted to  $f_{nat} = 17.1$  Hz ( $L = 10$  mm). The load impedance connected across 200 turns (second tap) is  $Z_L = (4.7 + j2\pi f 10.0 \times 10^{-6}) \Omega$ . The discrepancy between calculation and measurements is mainly due to low accuracy of analytical prediction of the spring constant  $k$  given by eqn (1) and measurement of damping coefficient  $\zeta$ .

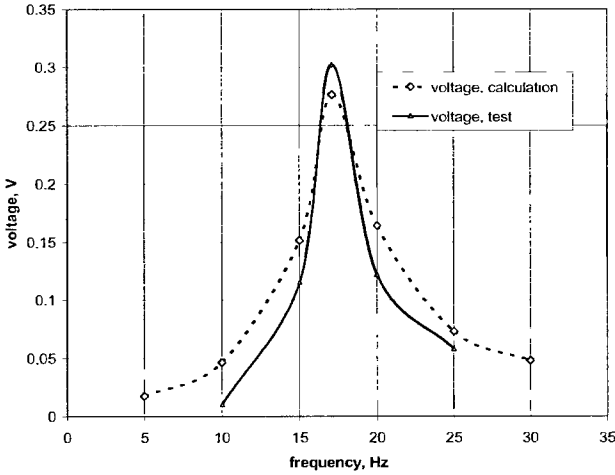


Fig 11. Comparison of the output voltage as a function of frequency obtained from calculations and measurements at natural frequency  $f_{nat} = 17.1$  Hz ( $L = 10$  mm), load impedance  $Z_L = (4.7 + j2\pi f 10.0 \times 10^{-6}) \Omega$ , and 200-turn coil impedance  $Z_i = (6.93 + j2\pi f 13.2 \times 10^{-6}) \Omega$ .

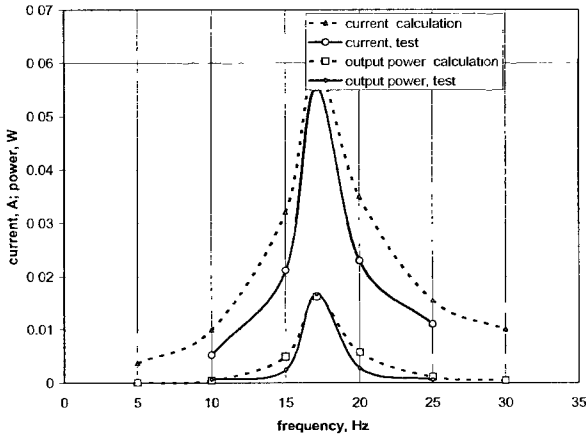


Fig 12. Comparison of the output *rms* current and output true power as a function of frequency obtained from calculations and measurements at natural frequency  $f_{nat} = 17.1$  Hz ( $L = 10$  mm), load impedance  $Z_L = (4.7 + j2\pi f 10.0 \times 10^{-6}) \Omega$ , and 200-turn coil impedance  $Z_i = (6.93 + j2\pi f 13.2 \times 10^{-6}) \Omega$ .

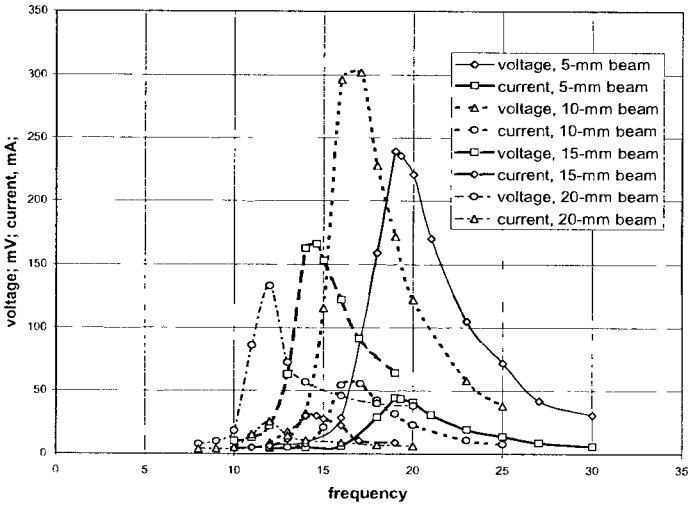


Fig. 13. Voltage and current versus frequency for different lengths of the steel spring (cantilever beam). Test results for load impedance  $Z_L = (4.7 + j2\pi f10.0 \times 10^{-6}) \Omega$ .

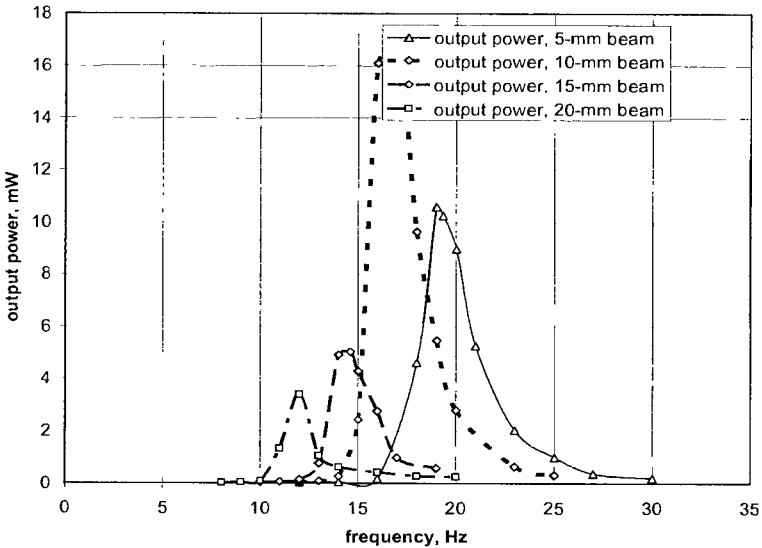


Fig. 14. Output power versus frequency for different lengths of the steel spring. Test results for load impedance  $Z_L = (4.7 + j2\pi f10.0 \times 10^{-6}) \Omega$ .

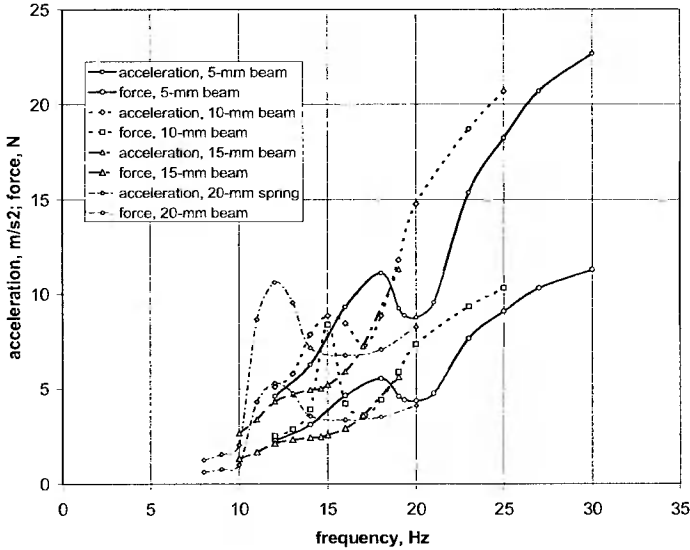


Fig. 15. Acceleration and accelerating force versus frequency for different lengths of the steel spring. Test results for load impedance  $Z_L = (4.7 + j2\pi f 10.0 \times 10^{-6}) \Omega$ .

Test results for different lengths of steel springs (cantilever beams) are shown in Figs 13, 14, and 15. The *rms* voltage and *rms* current versus frequency are plotted in Fig. 13. The maximum voltage and maximum current depend on the length of the spring. For the tested prototype the spring with the length of 10 mm (natural frequency  $f_n = 17.1$  Hz) at the load impedance  $Z_L = (4.7 + j2\pi f 10.0 \times 10^{-6}) \Omega$  provides the maximum voltage and maximum current. Consequently, for these parameters, the output power also takes its maximum value (Fig. 14). The power factor is high, very close to unity, because the load reactance is negligible. The linear acceleration and accelerating force (Fig. 15) are also very sensitive to the spring length.

## 7. SELF ADJUSTABLE DEVICE

In practice, the frequency  $f$  of vibration can change in wide range, usually from a few up to hundreds Hz, depending on the application. To maximize the efficiency of the energy harvesting electromechanical device, the natural frequency  $f_{nat}$  should be automatically adjusted to the frequency of vibration  $f$ . According to eqn (2) and Fig. 2, the simplest method is to control the length  $L$  of the cantilever beam (flat spring). This can be done by an electromechanical linear actuator and position control. If the frequency of vibration  $f$  increases, the length of the cantilever beam  $L$  should be reduced and extended if the frequency of vibration  $f$  decreases. There is no need for an additional sensor or encoder since the output frequency of the energy harvesting device can be used as a feedback signal.

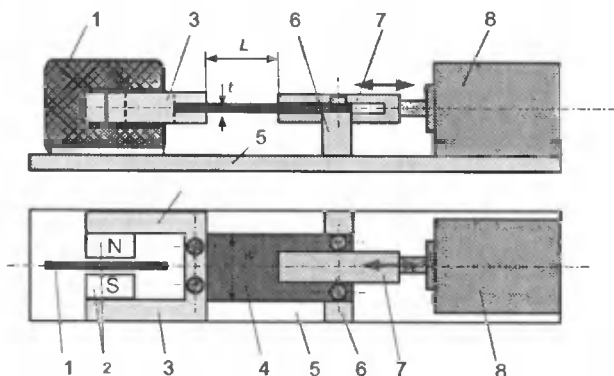


Fig. 16. Electromechanical energy harvesting device with adjustable cantilever beam: 1 – stationary coil, 2 – PMs, 3 – mild steel yoke (return path for magnetic flux), 4 – cantilever beam (flat spring), 5 – base, 6 – spring holder and guidance, 7 – U-shaped stabilizer, 8 – actuator [13].

Fig. 16 shows the energy harvesting electromechanical device with self-adjustable natural frequency of the spring-mass system [13]. The coil 1, PMs 2, magnetic circuit 3, cantilever beam 4, and base 5 are the same as in the case of constant natural frequency energy harvesting device presented in Fig. 1. One end of the adjustable cantilever beam 4 is permanently fixed to the support 6 which serves also as the guidance for the cantilever beam 4 and stabilizer 7. The U – shaped stabilizer 7 is driven by a linear actuator 8. The natural frequency of the cantilever beam is controlled by inserting the beam more or less into the slot of the stabilizer 7. The stiffness (thickness) of the stabilizer must be much higher than that of the cantilever beam, otherwise the adjustment of the natural frequency would be weak. The cantilever beam 4 is stationary while only the stabilizer is pushed towards the beam or pulled out in the opposite direction.

Even a powerful PM brushless or stepping linear motor may develop lower electromagnetic force density than a roller screw or ball lead screw actuator. This is why a linear actuator with rotary motor and roller screw or ball lead screw can provide better packaging than a direct drive linear PM brushless motor.

A linear PM motor consumes much more electrical energy than a linear actuator with rotary motor and roller or ball lead screw of similar rating. Although, direct drive linear motors provide more accurate positioning at higher speeds, these machines are characterized by much lower force density than linear actuators with rotary motors and roller or ball lead screws. In this case, a small size of the actuator and very low power consumption are extremely important.

The implementation of the control system for self-adjustment of the cantilever beam natural frequency is shown in Fig. 17. The transfer function of the energy harvesting device is expressed by eqn (25) in Appendix II. The frequency of the current in the coil is used as a feedback signal and then compared with the frequency of the source of vibration. The frequency error signal is amplified and the output current of the servo amplifier feeds the stator winding of the actuator.



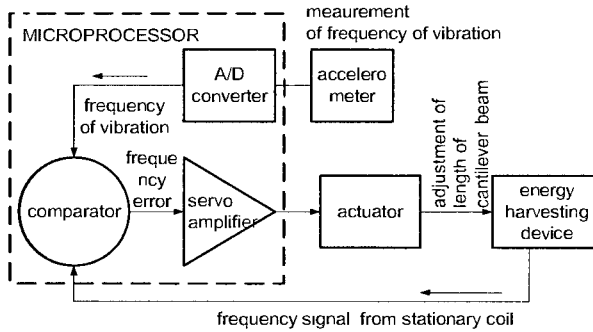


Fig. 17. Example of control circuit for adjustable cantilever length.

## 8. CONCLUSIONS

There is a physical limit imposed on the maximum output power of an electromechanical energy harvesting device with cantilever beam expressed by eqn (16). The output power is high when:

- the damping  $\zeta$ , natural frequency  $\omega_{nat}$ , tip mass  $M$ , and coil resistance  $R_c$  are low,
- the number of turns  $N$ , magnetic flux density  $B$ , length of magnets  $l_M$ , and amplitude of external force  $F_m$  are as high as possible.

The investigated energy harvesting electromechanical devices shows the following advantages:

- simple construction,
- provides low cost due to reduced number of parts, easy fabrication, and easy installation,
- high efficiency of conversion of vibrational energy into electrical energy in the case of adjustable length of cantilever beam (flat spring) and its natural frequency to the frequency of external vibration,
- eliminates external electrical power and wiring,
- ideal for sensors installed in tracks, trailers, and containers where the frequency of vibration is variable,
- ideal for sensors installed on rotating parts,
- the device is environmentally friendly,
- slip rings and induction loops are eliminated,
- the device is maintenance free – no battery replacement,
- high reliability;
- ability to scale down to MEMs level (micro-collisions, air friction dissipation, and cushioning effects must be included).

On the other hands, the designer of energy harvesting electromechanical devices must be aware of the following drawbacks and risks:

- Owing to application of electromechanical actuator and spring stabilizer, the volume of self-adjustable electromechanical energy harvesting device is bigger than that of an equivalent standard device that operates at constant natural frequency;

- Owing to application of high energy NdFeB PMs, there is a limit on ambient temperature. If ambient temperature exceeds 50 to 60°C, the performance, especially the output power, deteriorates;
- PMs can accumulate ferromagnetic particles and debris in the air gap area between poles and coil;
- The spring, spring support, and U – shaped stabilizer may require lubrication.

## APPENDIX I. MODELING OF VIBRATION OF CANTILEVER BEAMS BY ELEMENTARY BEAM THEORY

The static deflection of the cantilever beam as a function of the  $x$  coordinate is expressed as [4,5]:

$$x(y) = \frac{F_o}{6EI_a}(y^3 - 3Ly^2) \quad 0 \leq y \leq L, \quad (20)$$

where  $x$  is the deflection along the beam span  $y$ ,  $F_o$  is the tip load,  $E$  is Young's modulus,  $I_a$  is the area moment of inertia, and  $L$  is the beam length. The tip deflection  $\delta x(L)$  at  $y = L$  and corresponding spring constant  $k$  are

$$\delta = x(L) = -\frac{1}{3} \frac{F_o L^3}{EI_a} = -\frac{F_o}{k} \quad k = \frac{3EI_a}{L^3}. \quad (21)$$

The dynamics of vibration for given mode shape or characteristic deflection shape can be described by the following spring-mass equation, in which  $\delta(t)$  is a function of time  $t$ , i.e.:

$$m\ddot{\delta}(t) + k\delta(t) = F_o. \quad (22)$$

The above eqn (22) is an idealization of a cantilever beam [5]. Thus, the modal mass  $m$  in eqn (22) is not the same as the mass of the total cantilever beam  $m_b = \rho w t L$ . The modal mass can be obtained from the kinetic energy of the spring-mass system, i.e.:

$$E_k = \frac{1}{2} m \dot{\delta}^2(t) = \frac{1}{2} \left( \frac{33\rho w t L}{140} \right) \dot{\delta}^2 \quad (23)$$

The right hand side of eqn (23) has been found with the aid of eqns (20) and (21) [5]. The modal mass in eqn (22) is equal to (Fig. 22a):



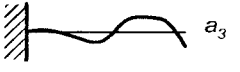
$$m = \left( \frac{33\rho w t L}{140} \right) = \left( \frac{33m_b}{140} \right) = 0.2357m_b, \quad (24)$$

Thus the vibration frequency for the modal shape  $n = 1$  of the modal eqn (18) is found as [5]:

$$\omega_1 = \sqrt{\frac{k}{m}} = a_1 \sqrt{\frac{EI_a}{\rho w t L^4}} \quad a_1 = 3.52 \quad (25)$$

Table 2 shows the first three vibration modes, modal mass, and coefficient  $a_n$  of a cantilever (clamped-free) beam. The values of coefficient  $a_n$  are according to [5].

Table 2. Transverse vibrations for cantilever beam.

vibration mode	modal mass	$a_n$
 $a_1$	$0.2357 m_b$	3.52
 $a_2$	$0.0062 m_b$	22.0
 $a_3$	$0.00079 m_b$	61.7

If a tip mass  $M$  is attached (Fig. 18b), the equation of motion (18) and spring constant (1) remain the same provided that the modal mass (20) is replaced by

$$m = 0.2357m_b + M \quad (26)$$

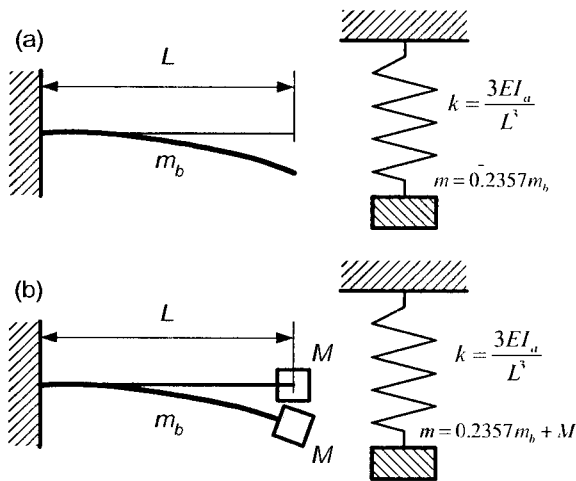


Fig. 18. Modeling cantilever beam by an equivalent spring-mass system: (a) without any tip mass; (b) with tip mass attached.

## APPENDIX II. TRANSFER FUNCTION AND TIME RESPONSE

The Laplace transform of eqn (6) is

$$m[s^2 X(s) - sx(0) - \dot{x}(0)] + c[sX(s) - x(0)] + kX(s) = F(s) \quad (27)$$

Assuming that the initial displacement and velocity are zero, i.e.,  $x(0) = \dot{x}(0) = 0$ , eqn (27) may be expressed as

$$G(s) = \frac{X(s)}{F(s)}; \quad G(s) = \frac{1}{ms^2 + cs + k}, \quad (28)$$

where  $G(s)$  is the transfer function (TF). The time-domain solution of the Laplace transform equation can be obtained by applying the inverse Laplace transform. For a unit impulse  $\lambda(s)=1$ , the time response expressed in seconds is:

$$x(t) = 2me^{-\left(\frac{c}{2m}\right)t} \frac{\sin\left(\frac{\sqrt{4mk - c^2}}{2m}t\right)}{\sqrt{4mk - c^2}}, \quad (29)$$

Fig. 19. shows the theoretical time response (29) for the tested energy harvesting device

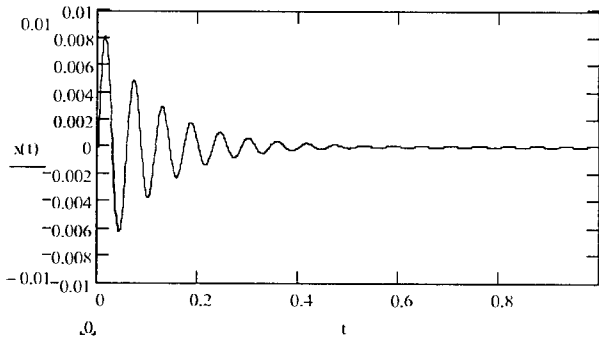


Fig. 19. Theoretical time response (seconds) for  $m = 0.083$  kg,  $k = 1005.4$  N/m,  $\omega_{nat} = 107.4$  rad/s ( $f_{nat} = 17.1$  Hz),  $c = 1.466$  kg/s, and  $\zeta = 0.08$ . Remaining data are given in Table 1.

## BIBLIOGRAPHY

- [1] Amirtharajah R., Chandrakasan A.P., 1998: *Self-Powered Signal Processing Using Vibration-Based Power Generation*, IEEE Journal of Solid State Circuits, Vol. 33, No. 5, 687-695.
- [2] Ching N.N.H., Wong H.Y., Li W.J., Leong, P.H.W. Wen, Z., 2002: *A laser-micro machined multi-modal resonating power transducer for wireless sensing systems*, Sensors and Actuators, Elsevier, vol. A 97-98, 685-690.
- [3] Choi H.Y., Jung S.Y., Jung H.K., 2002: *Performance Evaluation of Permanent Magnet Linear Generator for Charging the Battery of Mobile Apparatus*, Int. Conf. On Electr. Machines ICEM'2002, Brugges, Belgium, paper No 234 (CD).
- [4] Craig R.R., 1981: *Structural Dynamics: An Introduction to Computer Methods*, J. Wiley & Sons.
- [5] Den Hartog, J.P., 1984: *Mechanical Vibrations*, Dover Publications.
- [6] Glynne-Jones P., Tudor M.J., Beeby S.P., White N.M., 2004: *An electromagnetic, vibration-powered generator for intelligent sensor systems*, Sensors and Actuators, Elsevier, vol. A110, 344-349.
- [7] Lee J.M.H., Yuen S.C.L., Luk M.H.M., Chan G.M.H., Lei K.F., Li W.J., Leong P.H.W, Yam Y., 2003: *Vibration-to-Electrical Power Conversion Using High-Aspect-Ratio MEMS Resonators*, Power MEMS Conf., Chiba, Japan.
- [8] Meninger, S., Mur-Miranda, J.O., Amirtharajah, R., Chandrakasan, A.P., and Lang, H.J., 2001: *Vibration-to-Electric Energy Conversion*, IEEE Trans. on VLSI Systems, Vol. 9, No. 1, 64-76.

- [9] Shearwood C., Yates R.B., 1997: *Development of an Electromagnetic Microgenerator*, Electronics Letters, Vol. 33, No. 22, 1883-1884.
- [10] Shenck N.S., Paradiso J.A., 2001: *Energy Scavenging with Shoe-Mounted Piezoelectrics*, IEEE Micro, Vol. 21, No. 3, 30-42.
- [11] Sterken T., Baert K., Puers R., Borghs S.: *Power Extraction from Ambient Vibration*, Catholic University of Leuven, Leuven, Belgium.
- [12] Williams C.B., Yates R.B. 1995: *Analysis of a Micro-Electric Generator for Microsystems*, 8th Intern. Conf. on Solid-State Sensors and Actuators and Eurosensors IX, Stockholm, Sweden, 369-372.
- [13] Gieras J.F., Oh J.H., Huzmezan M.: *Electromechanical energy harvesting system*, Int. Patent Publ. WO 2007/044008 A1.

## ACKNOWLEDGMENT

This work has been sponsored by the United Technologies Corporation Fire and Security Program Office at UTRC, East Hartford, CT 06108, USA. Special thanks to Mr Tom Gillis, the Director of UTC Fire and Security Program Office for his support.

## PRZENOŚNE URZĄDZENIE ELEKTROMAGNETYCZNE DO POZYSKIWANIA ENERGII: ANALIZA ORAZ BADANIA EKSPERYMENTALNE

### Streszczenie

Artykuł omawia projektowanie, analizę oraz parametry urządzenia prototypowego do pozyskiwania energii, pracującego na zasadzie elektromechanicznego przetwarzania energii. Energia kinetyczna wejściowa w postaci energii wibracji mechanicznych jest przetwarzana na energię elektryczną (na zaciskach wyjściowych). Układ *sprężyna – masa* z ruchomym magnesem trwałym jest pobudzany mechanicznie przez wibracje zewnętrzne. Napięcie elektryczne jest indukowane w cewce stacjonarnej, na skutek wibracji biegunów magnesów trwałych. Kiedy cewka zostanie obciążona przez impedancję zewnętrzną, w obwodzie zewnętrznym popłynie prąd elektryczny proporcjonalny do wzniecającej SEM w cewce. Równania podstawowe do obliczania parametrów i charakterystyk zostały wyprowadzone na podstawie teorii elementarnej belki podpartej, analizy obwodowej oraz analizy polowej. Obliczenia teoretyczne zostały zweryfikowane pomiarami na zbudowanym prototypie.

Słowa kluczowe: pozyskiwanie energii, generator wibracyjny, elektromechaniczny, magnesy trwałe

## PRESENTATION OF THE DC MACHINE SIMULTANOUSLY BUT SEPARATELY CONTROLLED BY TWO VOLTAGES USING THE STATE-SPACE METHOD

Roman Żarnowski

Electrical Machines and Drives Group  
Department of Electrical Engineering,  
University of Technology and Life Sciences  
Al. S. Kaliskiego 7, 85-796 Bydgoszcz, Poland

*Summary:* The following paper presents the DC machine working as a motor, described by means of the state-space method. A computer model of the machine, compiled in the MATLAB/SIMULINK<sup>®</sup> environment is described as well. This model takes into account the phenomenon of dynamic inductance in the excitation circuit of the DC machine. This study presents also a comparison between the conventional (linearized) model and the model with a magnetization curve analytically approximated by the arc cotangent function. State trajectories are presented against a background of static characteristics occurring here in the form of a steady-state surface (SSS). The computer model compiled may be used to determine optimal control of these voltages in accordance with the quality coefficient employed.

Keywords: DC machine controlled by two voltages

### 1. INTRODUCTION

Modern methods of optimization are based on the state-space method [1,6], which excels over classic methods and holds many advantages. The classic control theory is convenient in designing a single input-output system. However modern control theory, which is based on the state-space method, allows for examination of systems subjected to control of signals pertaining to a broad class of input signals, not only in the impulse, step or sinusoidal form. As distinguished from classic methods, the state-space method allows for start and end conditions of the system. The vector-matrix notation simplifies solving of differential equations. However, apart from simple calculations, it is necessary to use a computer, what requires knowledge of numerical values of parameters of the object.

This article describes movement of a drive system based on a direct current motor by the means of the space-state method. For heed establishing, simulations were carried out for a test DC machine – model PZB632a with rated of nominal power 0.8 kW, armature voltage 220 V, armature current 4,6 A, excitation current 0,24 A and nominal rotations 1500 rpm. Simulations were prepared under the assumption of four load types occurring in engineering practice. During model assembly, almost all machine

parameters were varied, which allows modeling of a broad class of DC machines, from small machines up to large mine hoist motors. Results are presented in a new and unexpected manner, i.e. in the form of a steady-state surface (SSS). The state vector movement is presented against the background of this surface.

## 2. MATHEMATICAL MODEL

This model allows for taking into account the dynamic inductance phenomenon of the machine excitation circuit [2, 9]. It may, therefore, present an accurate description of the phenomena occurring in DC machine. However, simplifying assumptions does not make allowances for the following:

- a) a voltage drop across the brushes,
- b) inducing a flux screening the main flux under the influence of fast, dynamic changes of armature current,
- c) inaccuracies of machine compensation, and
- d) allowing for the character of the magnetization curve, (phenomenon of a machine magnetic core material hysteresis is omitted).

On the basis of the generalized machine model, the following DC machine equations were derived [8]:

$$\left. \begin{aligned} \frac{d\psi_{sd}(t)}{dt} &= U_{sd}(t) - \frac{1}{T_{sd}}\psi_{sd}(t) \\ \frac{d\psi_{wq}(t)}{dt} &= U_{wq}(t) - \omega(t)\psi_{wsd}(t) - \frac{1}{T_{wq}}\psi_{wq}(t) \\ \frac{d\omega(t)}{dt} &= \frac{1}{JL_{wq}}\psi_{wq}(t)\psi_{wsd}(t) - \frac{1}{J}M_{op}(t) \end{aligned} \right\} \quad (1)$$

The variable presented in these equations  $\psi_{wsd}$  can be formulated through  $\psi_{sd}$  as follows:

$$\psi_{wsd} = \frac{M_{wsd}}{L_{sd}}\psi_{sd} = \alpha\psi_{sd}, \quad (2)$$

where:

$\alpha$  – ratio, constant of the machine

$\psi_{sd}$  – stator flux linkage in d axis,

$\psi_{wq}$  – rotor flux linkage in q axis,

$\psi_{wsd}$  – stator in relation to the rotor flux linkage in d axis, and

$L_{wq}$ ,  $M_{wsd}$ ,  $T_{sd}$ ,  $\omega$ ,  $J$ ,  $M_{op}$  respectively: inductance of armature in q axis, inductance of armature in relation to stator in d axis, average time-constant of excitation circuit, angular velocity, moment of inertia, resistance torque.

For marking simplification, the following equations were assumed (Fig. 1.):

$$\left. \begin{aligned} \Psi_{sd} &= \Psi_m; U_{sd} = U_m \\ \Psi_{wq} &= \Psi_t; U_{wq} = U_t \\ L_{wq} &= L_t; T_{wq} = T_t \\ T_{sd} &= T_m \end{aligned} \right\} \quad (3)$$

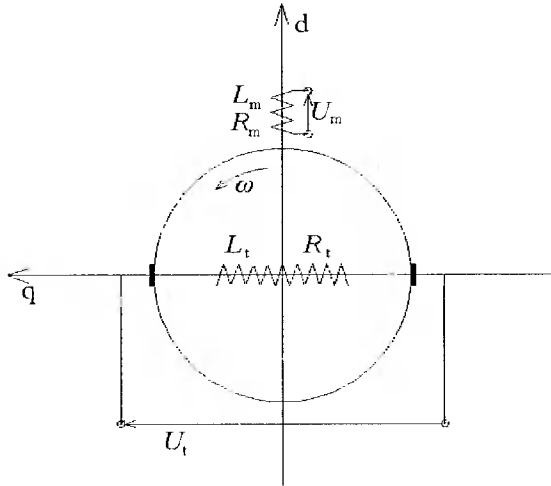


Fig. 1. DC machine diagram

Arranging equations (1) against new designations, the following results were acquired:

$$\frac{d}{dt} \begin{bmatrix} \Psi_m(t) \\ \Psi_t(t) \\ \omega(t) \end{bmatrix} = \begin{bmatrix} U_m(t) - \frac{1}{T_m} \Psi_m(t) \\ U_t(t) - \alpha \omega(t) \Psi_m(t) - \frac{1}{T_t} \Psi_t(t) \\ \frac{\alpha}{J L_t} \Psi_m(t) \Psi_t(t) - \frac{1}{J} M_{op}(t) \end{bmatrix}, \quad (4)$$

$$\frac{d}{dt} \begin{bmatrix} \Psi_m(t) \\ \Psi_t(t) \\ \omega(t) \end{bmatrix} = f(U_m(t), U_t(t), M_{op}(t), \Psi_m(t), \Psi_t(t), \omega(t)), \quad (5)$$

where:  $\mathbf{f} = \begin{bmatrix} f_1 \\ f_2 \\ f_3 \end{bmatrix}$  is a vector function of the abovementioned arguments, and

$\Psi_m(t), \Psi_t(t), \omega(t)$  are state vector coordinates. The nonlinear vector-matrix equation (4) constitutes a base for further considerations.



### 3. MODEL TECHNIQUE IN *SIMULINK*<sup>®</sup>

A comparison of two DC machine models is presented below. A simplified model was built with the assumption, that inductance of the excitation circuit is not undergoing alteration under the influence of the excitation current, and, therefore, is formed by equations (4).

State trajectory equations, allowing for dynamic inductance, were derived on the basis of the following procedure.

The abovementioned equation:

$$U_m = R_m i_m + \frac{d\Psi_m}{dt}, \quad (6)$$

after an analysis of a which DC excitation circuit with a ferromagnetic material, the magnetization curve was approximated by an arc cotangent curve of the following parameters  $a_0, a_1, a_2$ :

$$\Psi(i_m) = (a_0^* \cdot \arctg(a_1 i_m) + a_2^* i_m) \quad a_0^*, a_2^* = \frac{a_0}{\alpha}, \frac{a_2}{\alpha}, \quad (7)$$

assumes a new form:

$$\left. \begin{aligned} \frac{d\Psi_m}{dt} &= \left( \frac{a_0^* a_1}{1 + (a_1 i_m)^2} + a_2^* \right) \frac{di_m}{dt} \\ \frac{di_m}{dt} &= \frac{U_m - R_m i_m}{\frac{a_0^* a_1}{1 + (a_1 i_m)^2} + a_2^*} \\ \frac{di_m}{dt} &= \frac{(1 + (a_1 i_m)^2)(U_m - R_m i_m)}{a_0^* a_1 + a_2^* (1 + (a_1 i_m)^2)} \end{aligned} \right\} \quad (8)$$

Therefore:

$$\frac{d}{dt} \begin{bmatrix} i_m(t) \\ \Psi_t(t) \\ \omega(t) \end{bmatrix} = \begin{bmatrix} \frac{(1 + (a_1 i_m)^2)(U_m - R_m i_m)}{a_0^* a_1 + a_2^* (1 + (a_1 i_m)^2)} \\ U_t(t) - \alpha \omega(t) \Psi_m(t) - \frac{1}{T_t} \Psi_t(t) \\ \frac{\alpha}{J L_t} \Psi_m(t) \Psi_t(t) - \frac{1}{J} M_{op}(t) \end{bmatrix}. \quad (9)$$

Factors  $a_0$ ,  $a_1$ ,  $a_2$  were determined in the examination of the test machine. From the examination, a function course was directly assigned and assumed  $\alpha\psi_m = f(i_m)$ . The result of this trial is presented on Fig. 2.

Ratio  $\alpha$ , in the equations, was determined on the basis of the assumption that in the no-load conditions the following relationships are fulfilled:

$$\alpha = \frac{U_t - i_t R_t}{\omega \psi_m}; i_t = 0 \quad (10)$$

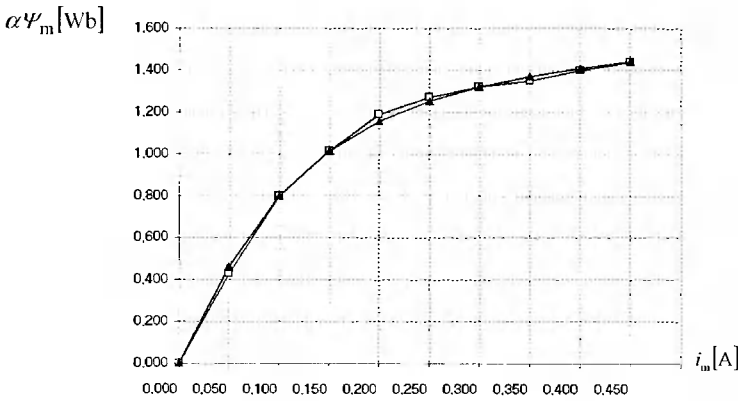


Fig. 2. Function course  $\alpha\psi_m = (a_0 \cdot \text{arctg}(a_1 i_m) + a_2 i_m)$ ; factors  $a_0$ ,  $a_1$ ,  $a_2$  amount to, respectively: 1.083; 9.078; 0.002.

The value of excitation circuit temporal constant  $T_{msr}$  might be accepted as an average, given by the manufacturer and amounting to 27ms for this machine. Then, for the machine considered,  $\alpha$  amounts to 0.3.

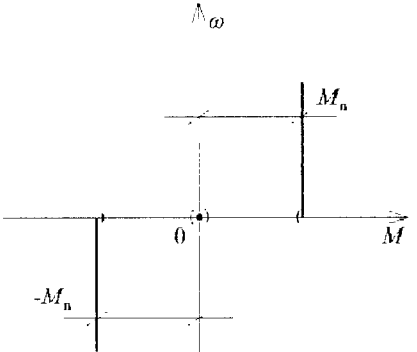
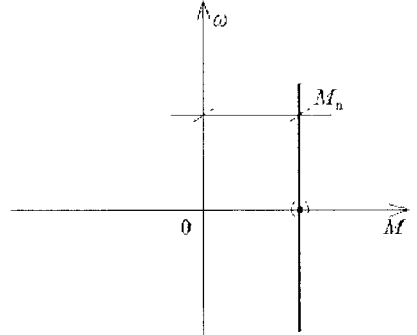
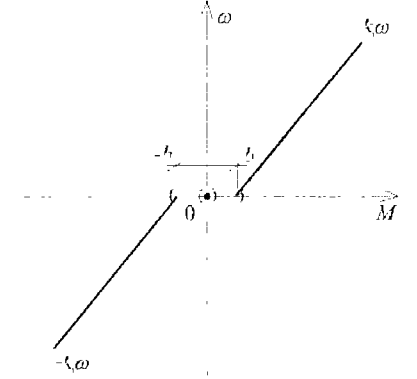
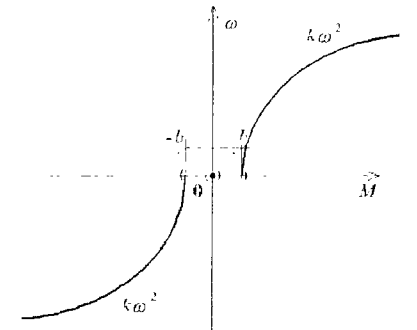
### 3.1. DISTURBANCES INFLUENCING MACHINE WORK

A number of disturbance classes influencing the machine were considered. The resistance torques, which frequently occur in engineering, are: active resistance torque, generator torque, fan torque, and constant passive torque. These four aspects of load torques may be described by one equation, the versions of which are presented below.

The shape and course of the SSS directly depends upon the course and values of a resistance torque on the shaft. Assuming that operation of a resistance torque, of one of the aforementioned aspects, occurs, it is possible to determine a state-space surface for each of them. Such an approach towards the matter indicates that a specified SSS corresponds to a resistance torque of a chosen class.

$$M(\omega) = \text{sign}(\omega) (b + a k \omega^\gamma), \quad \gamma \in \{0, 1, 2\}, \quad (11)$$

where: resistance torque load ratio  $a = \frac{M_{op}}{M_n}$ , value of initial friction torque  $b$ , factor of proportionality between resistance torque and angle velocity  $k$ .

Characteristic of torque	Equation	Type
	$M(\omega) = \text{sign}(\omega) a M_n$ $k = 1,$ $\gamma = 0,$ $b = 0,$ $M(0) = 0$	<p><b>Passive constant resistance torque</b></p>
	$M(\omega) = a M_n$ $k = 1,$ $\gamma = 0,$ $b = 0,$ $M(0) = M_n$	<p><b>Active constant resistance torque (crane torque)</b></p>
	$M(\omega) = \text{sign}(\omega)(b + a k_1 \omega)$ $k_1 > 0,$ $\gamma = 1,$ $b > 0,$ $M(0) = 0$	<p><b>Passive generator resistance torque</b></p>
	$M(\omega) = \text{sign}(\omega)(b + a k_2 \omega^2)$ $k_2 > 0,$ $\gamma = 2,$ $b > 0,$ $M(0) = 0$	<p><b>Passive fan resistance torque</b></p>

State trajectory depends on start and end conditions. The application, while altering voltage  $U_m$  and  $U_t$  in the external and internal loop enables plotting of these surfaces.

### The case of active resistance torque

$$\left. \begin{aligned} \psi_m &= a_0^* \cdot \operatorname{arctg}\left(\frac{U_m a_1}{R_m}\right) + a_2^* \frac{U_m}{R_m} \\ \psi_t &= \frac{L_1 M_{op}}{\alpha \psi_m} \\ \omega &= \frac{U_m - \psi_t \cdot T_t}{\alpha \psi_m} \end{aligned} \right\} \quad (12)$$

### The case of generator resistance torque and passive constant resistance torque ( $k_1 = 0$ , $b = M_{op}$ )

The SSS course of the active resistance torque proceeds according to the following equalities:

$$M_{op} = \operatorname{sign}(\omega)(b + ak_1\omega), \text{ where: } \operatorname{sign}(\omega) = \operatorname{sign}(U_m U_t) \quad (13)$$

Therefore:

$$\left. \begin{aligned} \psi_m &= a_0 \cdot \operatorname{arctg}\left(\frac{U_m a_1}{R_m}\right) + a_2 \frac{U_m}{R_m} \\ \psi_t &= \frac{L_1 \cdot \operatorname{sign}(U_m U_t)(b + ak_1\omega)}{\alpha \alpha_1} \\ \omega &= \left(1 + \frac{R_1 ak_1 \cdot \operatorname{sign}(U_m U_t)}{(\alpha \psi_m)^2}\right)^{-1} \left(\frac{U_t}{\alpha \psi_m} - \frac{R_1 b \cdot \operatorname{sign}(U_m U_t)}{(\alpha \psi_m)^2}\right) \end{aligned} \right\} \quad (14)$$

### The case of fan resistance torque

The SSS course of the active resistance torque was determined according to the following equations:

$$M_{op} = \operatorname{sign}(\omega)(b + ak_2\omega^2) \quad (15)$$

Finally:

$$\left. \begin{aligned} \psi_m &= a_0^* \cdot \operatorname{arctg}\left(\frac{U_m a_1}{R_m}\right) + a_2^* \frac{U_m}{R_m} \\ \psi_t &= \frac{L_1 \cdot \operatorname{sign}(U_m U_t)(b + ak_1 x_3)}{\alpha \alpha_1} \\ \omega &= \frac{-1 + \operatorname{sign}(U_m U_t) \sqrt{4pq + 1}}{2p} \end{aligned} \right\} \quad (16)$$

where:

$$\text{sign}(\omega) \frac{R_i a k_s}{(\alpha^2 \Psi_m)^2} = p,$$

$$\frac{U_s}{\alpha^2 \Psi_m} - \frac{R_i \cdot \text{sign}(\omega) b}{(\alpha^2 \Psi_m)^2} = q$$

The first coordinate of the state vector  $\Psi_m$  indicates the linkage flux in the excitation circuit and, the state trajectory, allowing for dynamic inductance, is calculated [7] in relation to magnetizing current  $i_m$ . It is necessary, therefore, to establish initial conditions of the integrator, in relation to this current. The current  $i_m$  determination for the given  $\Psi_m$  from equation (8) is not possible due to function implisiting. In this case, for the given current,  $\Psi_m$  the value of the current  $i_m$  is determined iteratively each time on the basis of the following calculation:

$$\Psi_m = a_0^* \cdot \text{arctg} \left( \frac{U_m a_1}{R_m} \right) + a_2^* \frac{U_m}{R_m} \quad (17)$$

After appropriate conversions we have equation:

$$\text{tg} \left( \frac{\Psi_m - a_2^* i_m}{a_0^*} \right) - a_1 i_m = \varepsilon_m \quad (18)$$

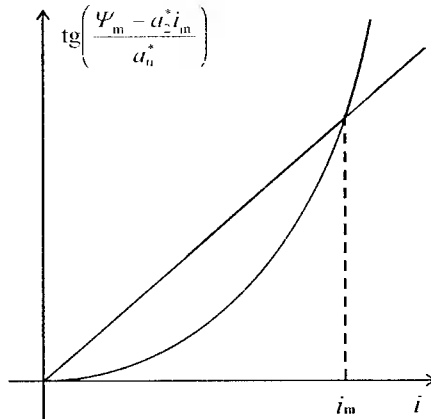


Fig. 3. Interpretation of iterative method of magnetizing current determination, accurate to  $\varepsilon_m$  (here employed accuracy of: 0.0000001)

Solving this allows for creating a model [3, 4, 5], which, as author argues, presents courses of a real DC machine in a rather accurate manner.

The block diagram in *SIMULINK*<sup>®</sup> corresponding to the vector equation of state trajectory (9)

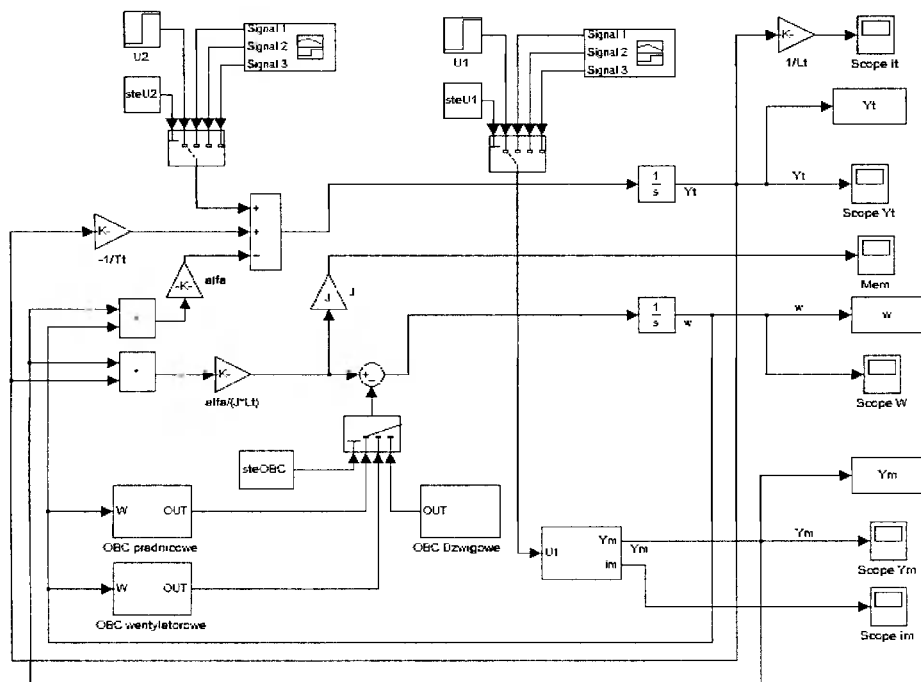
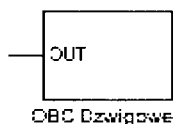


Fig. 4. Block diagram of the DC machine allowing for dynamic inductance of excitation circuit, where  $Y_t = \Psi_t$ ,  $Y_m = \Psi_m$ ,  $w = \omega$ .

Diagrams included in blocks.



This element includes a hidden diagram presented in Fig. 5.

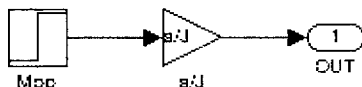
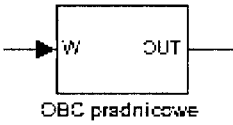


Fig. 5. Active resistance torque simulation diagram.



This element includes a hidden diagram presented in Fig. 6.

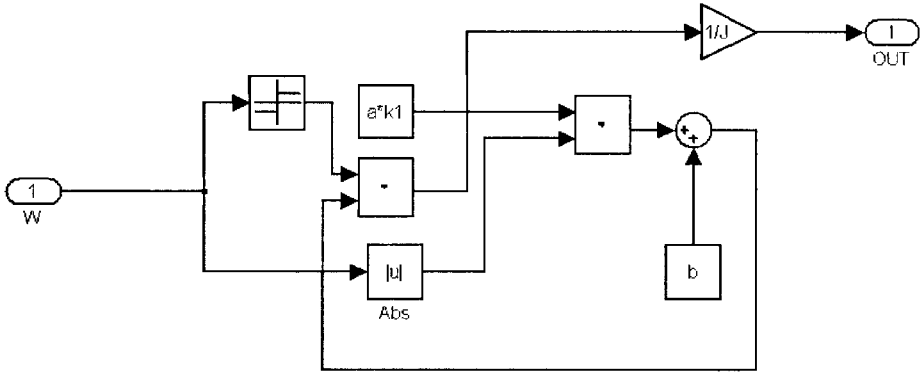
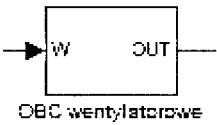


Fig. 6. Generator torque simulation diagram.



This element includes a hidden diagram presented in Fig. 7.

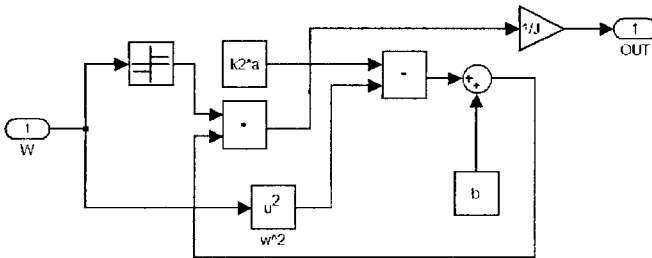
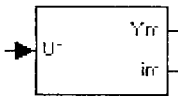


Fig. 7. Fan torque simulation diagram.



The block contains the first trajectory equation for the case taking into account dynamic inductance. The input quantity is a signal of  $U_m$ , the output signals are:  $\Psi_m$  and  $i_m$ . The internal diagram is presented in Fig. 8.

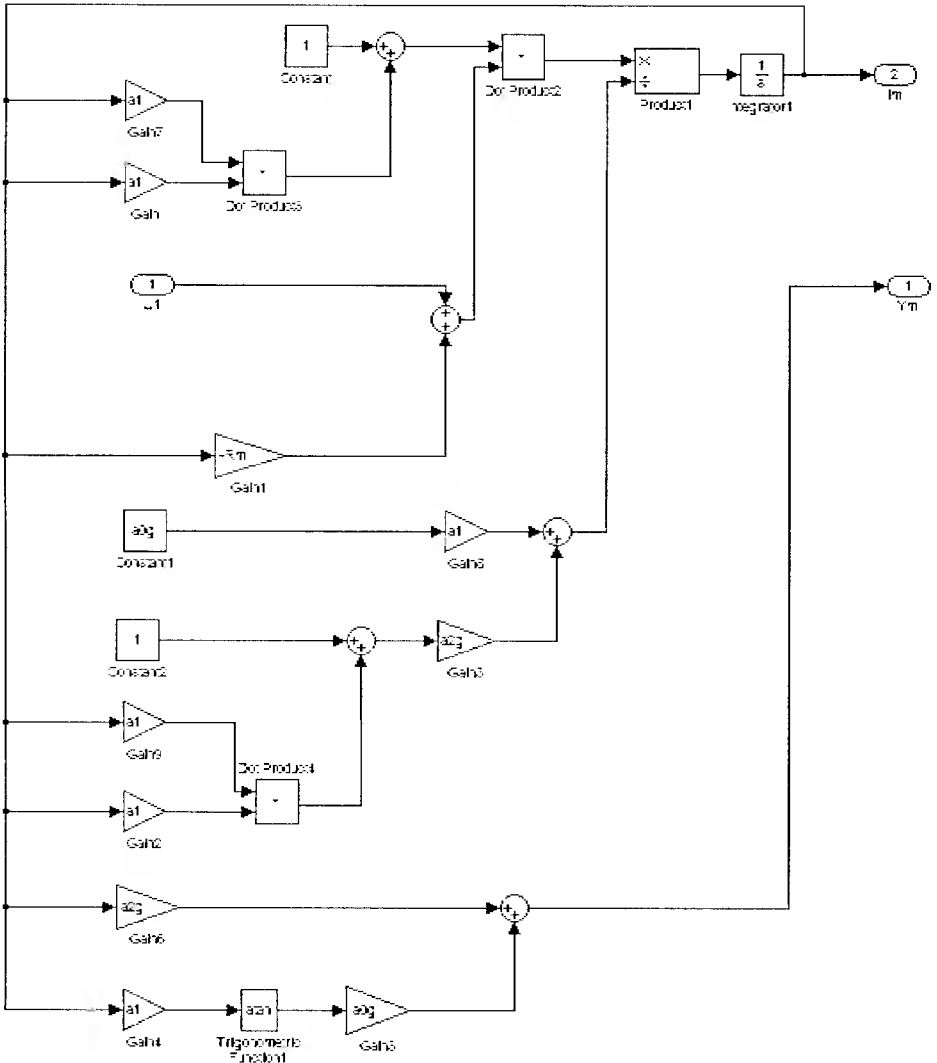


Fig. 8. Excitation circuit simulation diagram of the DC machine allowing for dynamic inductance of excitation circuit.





Diagram parameters used in calculations are listed in the following table:

Parametry Maszyny

PARAMETRY MASZYN

Mn [Nm] =	5.1
Rm [Ohm] =	726.29
Lt [H] =	0.01264
Rt [Ohm] =	4.28
Tm [s] =	0.019
U1n [V] =	230
U2n [V] =	230
alfa =	0.3
a0 =	1.0627
a1 =	9.0783
a2 =	0.002
J [kgm <sup>2</sup> ] =	0.010039
a (Mop=a*Mn) =	1
b (Mt=b*Mn) =	0.05
k1 [Nms] =	0.034
k2 [Nms <sup>2</sup> ] =	0.000226
U1 [V] =	0
U2 [V] =	0
steOBC (1-P,2-W,3-D) =	1
steU1 (1,2,3,4) =	1
steU2 (1,2,3,4) =	1
cw (1-1cw 2-4cw) =	1

OK and run

load

Rated torque  
 Effective resistance of excitation circuit  
 Inductance of armature circuit  
 Effective resistance of armature circuit  
 Aver. time-constant of excitation circuit  
 Final excitation voltage  
 Final armature voltage

Ratio, constant of the machine acc. to eq.(2)  
 Magnetization curve shape fac.  
 Magnetization curve shape fac.  
 Magnetization curve shape fac.

Inertia moment of drive  
 Relative load torque  
 Relative load of an initial friction passive torque

Gen. torque factor acc. to Fig. 5  
 Fan torque factor acc. to Fig. 6

Initial value of excitation volt.  
 Initial value of armature volt.  
 Load type choice (1- generator, 2- fan, 3- crane)  
 Excitation voltage - choice of function course  
 Armature voltage - choice of function course  
 Chart illustration method choice (1 - in the first quarter, 2 - in four quarters)

Fig. 10. Method of introducing DC machine data to the simulation program.

## 4. DESCRIPTION OF SIMULATIONS

The test was performed by using the machine parameters obtained from laboratory studies. However, it is necessary to stress that this model is general enough to allow simulation and examination of any given DC machine.

The 3D chart presents the SSS in Fig. 15. Its color depends on the quarter in which the panel was placed; first quarter – red ( $U_{m+} + i U_{r+}$ ); second quarter – yellow ( $U_{m+} + i U_{r-}$ ); third quarter – blue ( $U_{m-} + i U_{r-}$ ); fourth quarter – green ( $U_{m-} + i U_{r+}$ ). The blue line in the chart presents the state trajectory. The next charts also present courses of each vector components versus time function.

### Comparison of DC motor allowing for dynamic inductance in excitation circuit to DC machine allowing for static inductance

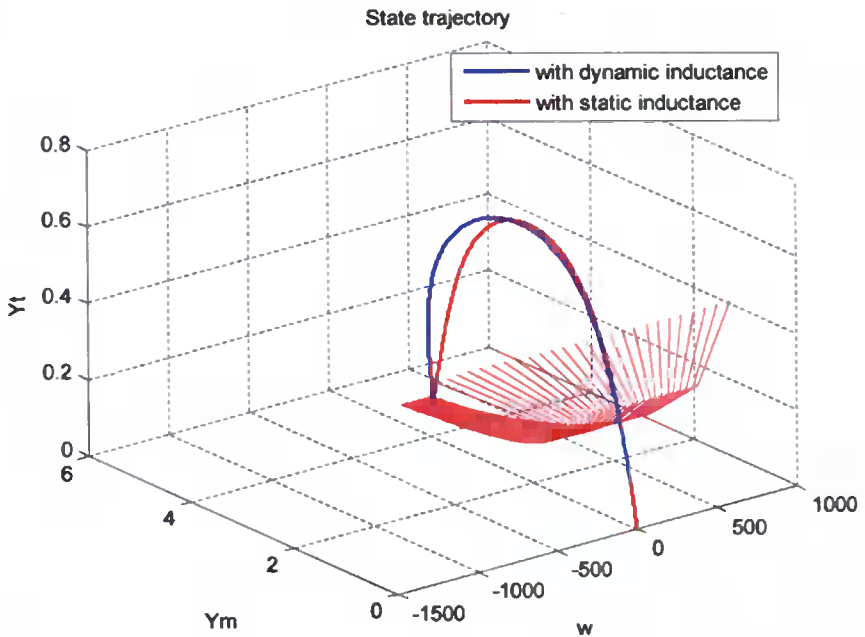


Fig. 11. Result of simulation comparison of a linearised model and a model allowing for changing inductance during start-up.

Fig. 11 presents the results of a comparison between two motor models, based on the trajectory course of the state, during machine start-up. While the red line is the course of the state vector, not allowing for excitation circuit dynamic inductance, the blue line is the response of the system allowing for nonlinearity of the magnetization curve in the machine magnetic core. The results of modeling were inserted for comparison purposes. Although static values of the state vector are the same, the transients differ from each other. Therefore, the model with dynamic inductance of the excitation circuit was assumed for further consideration.

The state trajectory of a motor, loaded with generator passive resistance torque, when start voltages are equal to  $U_m = -100, U_t = -100$  V and end voltages are equal to  $U_m = 230, U_t = 230$  V, is presented in Fig.12. Load torque is equal to rated motor torque.

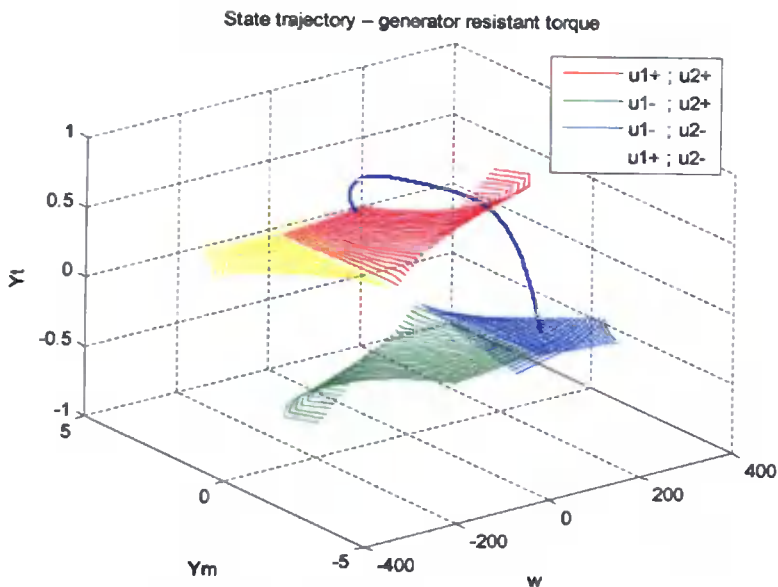


Fig. 12. State trajectory loaded with generator passive resistance torque, with initial voltages equal to  $U_m = -100$  V,  $U_t = -100$  V and end voltages equal to  $U_m = 230$  V,  $U_t = 230$  V presented in four quarters of the state surface. Load torque in steady state is equal to rated motor torque.

The state vector components alter the value of  $\Psi_m$  and  $\Psi_t$  from negative to positive. The shape of the SSS allows that the motor be loaded with the generator passive resistance torque. Courses of the state vector components  $\Psi_m$ ,  $\Psi_t$  and  $\omega$ , and useful variables such as armature current  $i_t$  and magnetizing current  $i_m$  are presented on figures 13÷16.

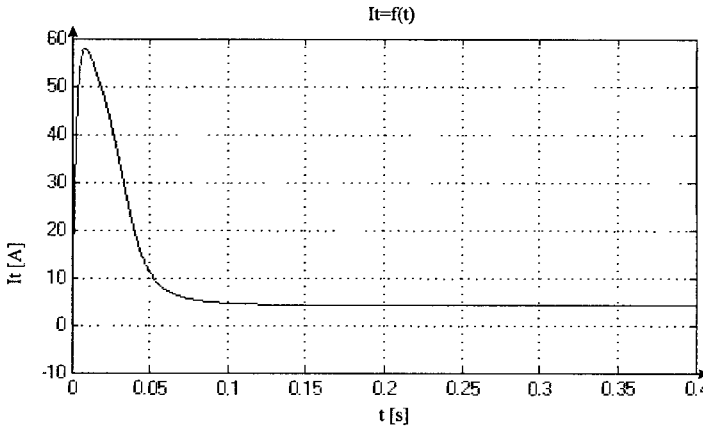


Fig. 13. Armature current course  $i_t = f(t)$ ; machine loaded with generator passive resistance torque, with start voltages equal to  $U_m = -100$  V,  $U_t = -100$  V, and end voltages equal to  $U_m = 230$  V,  $U_t = 230$  V. Torque in steady state is equal to rated motor torque.

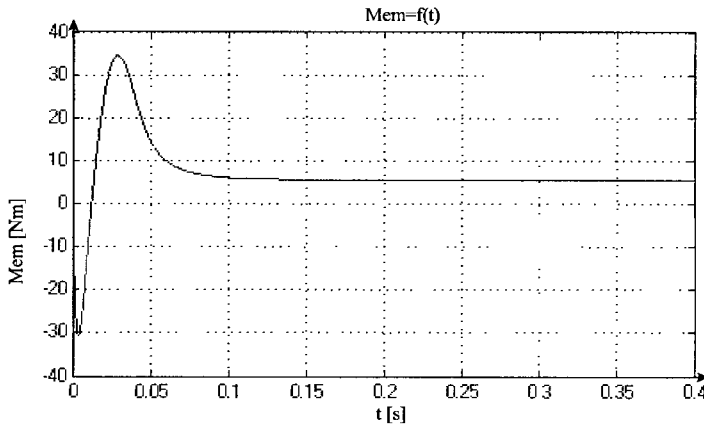


Fig. 14. Armature current course  $M_{em} = f(t)$ ; machine loaded with generator passive resistance torque constant, with initial voltages equal to  $U_m = -100$  V,  $U_t = -100$  V, and end voltages equal to  $U_m = 230$  V,  $U_t = 230$  V. Load torque is equal to rated motor torque.

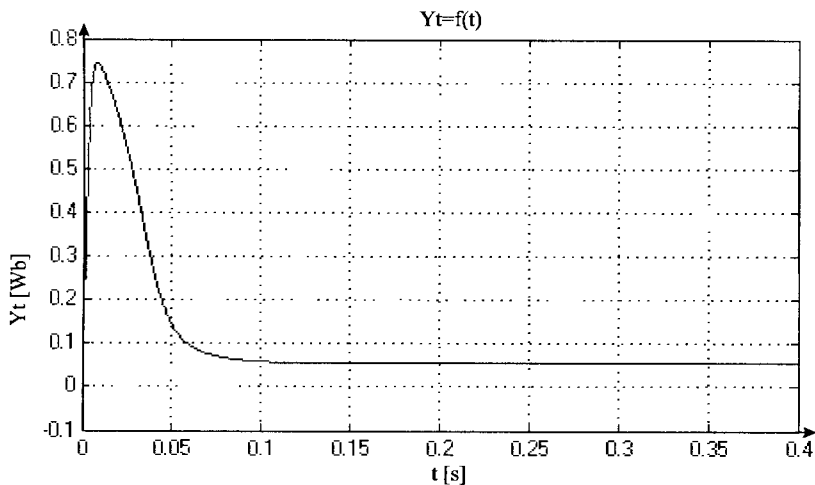


Fig. 15. Armature linkage flux course  $\Psi_t = f(t)$ ; machine loaded with generator passive resistance torque, with initial voltages equal to  $U_m = -100$  V,  $U_t = -100$  V, and end voltages equal to  $U_m = 230$  V,  $U_t = 230$  V. Load torque is equal to rated motor torque

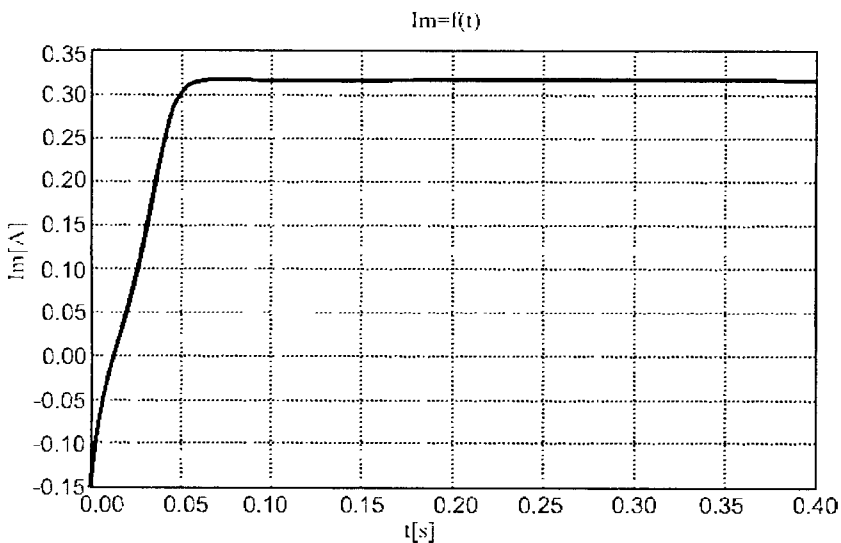


Fig. 16. Magnetizing current course in excitation circuit  $i_t = f(t)$ ; during voltage alteration from -100V up to 220V. Approximated magnetizing curve is allowed

Another example of DC motor state trajectory loaded with nominal active resistance torque in steady state, with initial voltages equal to  $U_m = 120$ ,  $U_t = 120$  V, and end voltages equal to  $U_m = 230$ ,  $U_t = 230$  V is presented in Fig. 17.

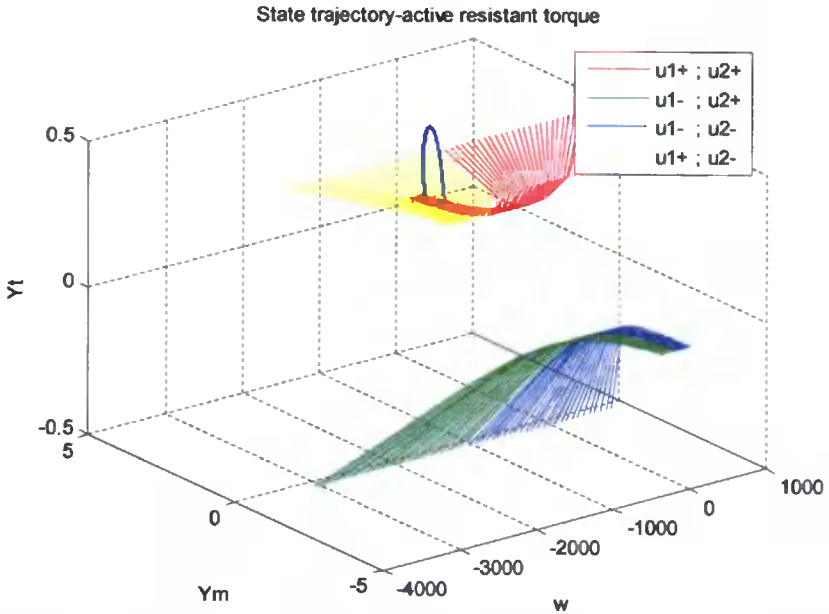


Fig. 17. State trajectories loaded with active resistance torque with start voltages  $U_m = 120, U_t = 120$  V, and end voltages  $U_m = 220, U_t = 220$  V presented in four quarters of the state surface. Load torque is equal to rated motor torque.

## 5. CONCLUSION

The article presents results of DC machine simulation based on the independent DC machine simulator, which is developed by the author. It has been illustrated, that the space-state method used in this simulations allows:

- magnetizing curve of this machine to be nonlinear. (approximated by arc cotangent function),
- introduce the dynamic inductance into DC machine excitation circuit calculations,
- to point noticeable differences in the state trajectory course between a linearized and nonlinear machine model,
- to find future methods for optimal motor control in accordance with the employed quality coefficient.

More-over,

- the state-space surface SSS is composed of four panels and it creates static characteristics in 3D space,
- courses of currents, linkage fluxes and angle velocity of the machine obtained on the basis of simulations confirm the courses available in literature.

This model is universal and enables carrying out simulations loaded with all types of basic load encountered in engineering practice. Motors from small up to large hoist ones, can be simulated, while making allowances for simplification of assumptions.

## BIBLIOGRAPHY

- [1] Athans M., Falb P.L., 1966: *Sterowanie optymalne*, WNT Warszawa.
- [2] Hassane M., Djuoza S., Boudjemaa T., 1998: *Identification Parameters Method For DC machine Including Friction*. Power Electronics And Variable Speed Drives 21-23 Sept. 1998, Conf. Publication No 456, IEE.
- [3] Liang Y.C., Gosbell V., 2006: *Realistic Computer Model of DC Machine for CADA Topology on SPICE2*. School of Electrical Engineering. The University of Sydney, NSW, Australia [in] IEEE.
- [4] Liang Y.C., Gosbell V., 1990: *DC Machine Models for SPICE2 Simulation*. IEEE Trans. On Power Electronics, vol. 5. No 1.
- [5] Mrozek B., Mrozek Z., 2004: *Matlab i Simulink - poradnik użytkownika*, Wydawnictwo HELION, Gliwice.
- [6] Ogata K., 1976: *Metody przestrzeni Stanów w teorii sterowania*, WNT, Warszawa.
- [7] Stachurski M., 2003: *Metody numeryczne w programie Matlab*, Wydawnictwo MIKOM, Warszawa.
- [8] Stein Z., 1971: *Maszyny elektryczne w automatyce*, Wydawnictwo Uczelniane Politechniki Poznańskiej, Poznań.
- [9] Trutt F.C., Erdpilyi E.A., Hopkins R.E., 1968: *Representation of the Magnetization Characteristic of DC Machines for Computer Use*. IEEE Transactions on Power Apparatus And Systems, vol. PAS-87, No. 3.

PRZEDSTAWIENIE MASZYN PRĄDU STAŁEGO  
STEROWANEJ JEDNOCZEŚNIE DWOMA NAPIĘCIAMI  
METODĄ PRZESTRZENI STANU

Streszczenie

W pracy przedstawiono maszynę DC pracującą jako silnik, opisaną metodą przestrzeni stanu. Zaprezentowano model komputerowy napisany przy pomocy programu MATLAB/SIMULINK<sup>®</sup>. Model ujmuje zjawisko indukcyjności dynamicznej obwodu wzbudzenia maszyny. Trajektorie stanu przedstawiono na tle charakterystyk statycznych występujących tu w postaci powierzchni stanów ustalonych (PSU). Ponadto porównano model konwencjonalny (zlinearyzowany) z modelem o charakterystyce magnesowania przybliżonej analitycznie funkcją arcustangens. Opracowany model komputerowy może zostać wykorzystany do wyznaczenia sterowania optymalnego, niezależnie dwoma napięciami, według przyjętego wskaźnika jakości.

Słowa kluczowe: maszyna DC sterowana jednocześnie dwoma napięciami



ISSN 0209-0570